Chapter 2
Raman Spectroscopy: Characterization of Edges, Defects, and the Fermi Energy of Graphene and sp^2 Carbons

M.S. Dresselhaus, A. Jorio, L.G. Cançado, G. Dresselhaus, and R. Saito

Abstract From the basic physical concepts relating to the Raman spectra of graphene, we can develop characterization methods for point defects and the edge structure. Furthermore, the Fermi energy can be studied by the phonon softening phenomena of the Raman spectra. Finally, we also discuss recent progress on near-field optics.

2.1 Introduction to the Resonance Raman Spectra of Graphene

Raman spectroscopy has been widely used to characterize sp^2 carbon systems, from graphite to carbon nanotubes. Especially interesting is the richness of the Raman spectral response to lattice symmetry breaking and to changes in the Fermi level. These two aspects are very important when moving from bulk 3D materials down to nanomaterials, where single defects, edges, and interactions with the environment become frequent and important. In this scenario, two-dimensional (2D) graphene becomes an important prototype system to study such effects, as we discuss in this chapter. We start by giving, in this section, introductory material with the basic concepts behind the Raman spectroscopy of sp^2 carbon systems.

M.S. Dresselhaus (✉)
Department of Physics, Department of Electrical Engineering and Computer Science, Massachusetts Institute of Technology, Cambridge, MA 02139-4307, USA

A. Jorio · L.G. Cançado
Departamento de Física, Universidade Federal de Minas Gerais, Belo Horizonte - MG, 30123-970, Brazil

G. Dresselhaus
Massachusetts Institute of Technology, Cambridge, MA 02139-4307, USA

R. Saito
Department of Physics, Tohoku University, Sendai 980-8578, Japan

H. Raza (ed.), *Graphene Nanoelectronics*, NanoScience and Technology,
DOI 10.1007/978-3-642-22984-8_2, © Springer-Verlag Berlin Heidelberg 2012

UNCORRECTED PROOF

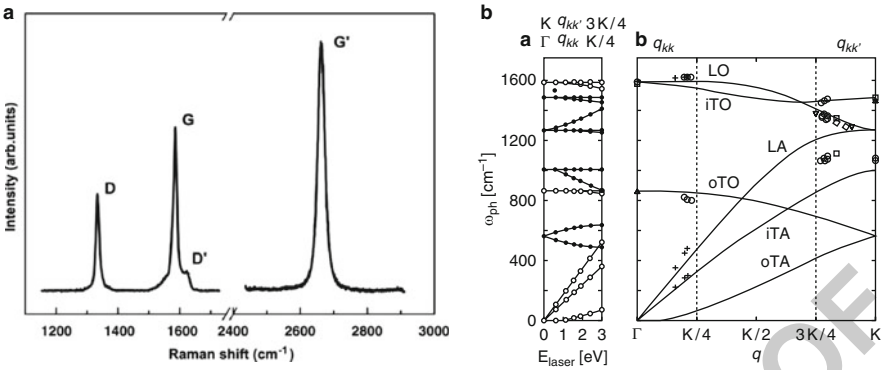

Fig. 2.1 (**a**) Raman spectrum of a graphene edge, showing the main Raman features, the D, G, D', and G' bands taken with a laser excitation energy of 2.41 eV [1]. (**b**) On the *left* are the calculated Raman frequencies for the double-resonance condition in graphene as a function of E_{laser} (bottom horizontal axis) and the corresponding q vector along the K (top horizontal axis). *Solid and open circles* correspond to phonon modes around the K and Γ points, respectively. The q_{KK} vectors from Γ to $K/4$ are shown by *open circles* and the q_{KK} vectors from $3K/4$ to K are shown by *solid circles*. The six calculated phonon dispersion curves (*lines*) and experimental Raman observations (*symbols*) are plotted and shown to be consistent with double resonance theory [2]

2.1.1 *The Raman Spectra of sp^2 Carbons*

The Raman spectrum of crystalline graphite is characterized by the presence of two strong symmetry-allowed peaks at 1,580 and 2,700 cm^{-1}, the G and G' bands, respectively, where the G label refers to spectral features[1] originating from graphene (see Fig. 2.1). The G band is a first-order Raman signal originating from the zone-centered, in-plane optical-phonon modes as shown in Fig. 2.1a as a spectral feature, while Fig. 2.1b shows that the G'-band phonon has a frequency near 1,600 cm^{-1} and a very small wave vector q often approximated as $q = 0$ [3, 4]. Because graphene is a zero-gap semiconductor, there is a strong electron–phonon interaction. We will see in Sect. 2.1.5 that because of this strong electron–phonon interaction the $q = 0$ G-band phonon, and consequently the G-band phonon frequency, intensity, and lineshape are strongly dependent upon doping. The G' band is a second-order, two-phonon feature that is specially strong in sp^2 carbons. The G' band is important for many reasons, due to the fact that the G' depends upon the phonon wave vector q and allows study of the electronic structure of sp^2 carbons through study of their phonons [5, 6]. Many of the unusual properties of the G' band arise from the mechanism responsible for the large intensity of the G' band, which is a multiple resonance process. These topics are further clarified in Section 2.1.5.

[1] In this chapter, we frequently use the word "feature" to refer to spectral features. For example, "The first-order Raman feature" means that the Raman spectral line originates from a first-order Raman scattering process.

UNCORRECTED PROOF

Disorder-induced symmetry-breaking effects are important in the determination of several material properties, such as transport properties and the relaxation of photoexcited carriers [7, 8]. This applies specially to sp^2 carbons, which have high symmetry and, consequently, are highly sensitive to symmetry-breaking defects. Raman spectroscopy is particularly sensitive to symmetry-breaking phenomena in sp^2 carbons. Thus Raman spectroscopy is widely used to identify the presence of defects and disorder in sp^2 networks of different carbon structures, such as diamond-like carbon, amorphous carbon, and nanostructured carbon, as well as carbon nanofibers, nanotubes, nanohorns and most recently graphene [9–12].

In the Raman spectra obtained from graphene and other sp^2 carbon samples containing defects, several additional symmetry-breaking features are found. The feature with highest intensity is the D band which occurs near 1,350 cm^{-1} for laser excitation energies of 2.41 eV (a commonly used laser excitation energy) and the D band is associated with near-K point phonons. Another common symmetry-breaking feature in the first-order spectrum is the D' band near 1,620 cm^{-1}, associated with near-Γ ($q \neq 0$) point phonons, where q refers to the phonon wave vector. The D and D' bands can also give rise to overtones and combination modes, thereby resulting in additional symmetry-breaking modes in the Raman spectra. Now we give a brief description of the wave vectors for these modes.

The D band is associated with a breathing-like motion of the carbon atoms located in carbon hexagons that becomes Raman active due to the loss of the lattice symmetry. The most common reasons for symmetry breaking are the presence of vacancies and interstitial or substitutional atoms which can also be introduced intentionally as for example by ion implantation [13] or by introducing interfaces at the borders of crystalline areas [3, 4]. The frequency of the D band is about half of the second-order G' frequency ($\omega_{G'}/2$). The mechanism involved in the G'-band process is a symmetry-allowed two-phonon process that is also present in ideally crystalline graphene. However, the $\sim$1,350 cm^{-1} D-band peak is only observed in the presence of defects or at the edge of a graphene sample in an otherwise perfect infinite graphene structure. The intensity of the D band is proportional to the amount of disorder (as, for example, at a point defect or at a crystallite boundary) in the sample. The ratio between the intensities of the disorder-induced D band and the first-order graphite G band (I_D/I_G) provides a parameter that can be used for quantifying the amount of disorder.

Tuinstra and Koenig showed in 1970 that the I_D/I_G intensity ratio [3, 4] is correlated with the crystallite size L_a by the relation $I_D/I_G = A/L_a$, where A is a constant for a fixed laser excitation energy E_{laser}.[2] This means that the I_D/I_G intensity ratio depends on the laser excitation energy E_{laser} [14]. The Tuinstra and Koenig relationship has been frequently used to characterize carbon sp^2 crystallites large enough to have a well-established graphene-like structure. On the other hand, Lucchese et al. showed recently that in the limit of amorphization, the ratio I_D/I_G

[2]This means that A changes for different E_{laser} and we cannot directly compare the I_D/I_G values of two different samples observed by two different values of E_{laser}.

UNCORRECTED PROOF

decreases as the crystallite goes down to very small L_a values [15]. In this limit, the sp^2 carbon hexagonal crystal structure for graphene is not well defined.

The so-called D' band, centered at 1,620 cm^{-1}, is usually observed in the Raman spectra of graphene and other disordered sp^2 carbon materials, although the D' band has a weaker intensity when compared to the D band. The D' band feature, reported in 1978 by Tsu et al. [16], also depends on L_a and E_{laser} [10] but involves a different scattering process. The D band involves an intervalley scattering process, as explained below, while the D' band involves an intravalley scattering process [17].

Vidano et al. showed in 1981 [18] that the D and G' bands are dispersive, i.e., their Raman shift frequencies change with E_{laser} according to the relations $\Delta\omega_D/\Delta E_{\mathrm{laser}} \sim 50\,\mathrm{cm}^{-1}/\mathrm{eV}$ and $\Delta\omega_{G'}/\Delta E_{\mathrm{laser}} \sim 100\,\mathrm{cm}^{-1}/\mathrm{eV}$. The out-of-plane stacking order has also been shown to affect the G'-band Raman lineshape and intensity [19–21]. The explanation for the exceptionally large dispersive behavior of both the D band and G' band as well as the large G'-band intensity came in 2000, through the work of Thomsen and Reich [22], and their model described in Section 2.1.3 was extended by Saito et al. to explain the mechanism behind many other dispersive Raman peaks observed in the Raman spectra [17,23] of sp^2 carbon materials.

2.1.2 Edge Structure of Graphene

In the characterization of defects of graphene, the edges are the dominant source of defect-related features in the Raman spectra. There are two symmetrical edge structures, armchair and zigzag edges (see Fig. 2.2). The general structure of edges are random but we can treat the general edge as a mixture of zigzag and armchair edges. When we heat a graphene sample to more than 2,000°C in an electron microscope in the presence of the electron beam, the armchair and zigzag edge structures become increasingly dominant and especially the zigzag edges are observed predominately at the highest heat treatment temperatures [24]. In such samples, the more general chiral edges tend to break up into small segments of zigzag and chiral edges (see Fig. 2.2) [25,26]. Characterization of the edge structure by Raman spectroscopy and the related theory is discussed in Sect. 2.3.

AQ3

2.1.3 The Multiple-Resonance Raman Scattering Process

Both the D band and the D' band are double-resonance processes, as briefly described below, except that the D band involves an intervalley scattering process from the K point to the K' point in the Brillouin zone, whereas the D' band is an intravalley scattering process involving wave vectors q located near the same K point or the same K' point in reciprocal space [see Fig. 2.3a].

UNCORRECTED PROOF

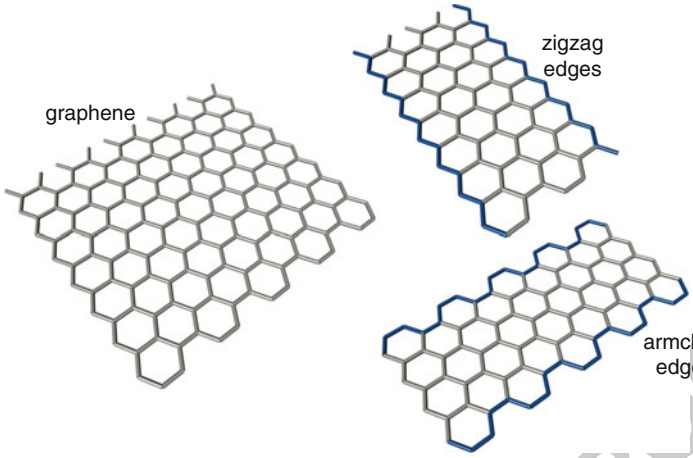

Fig. 2.2 Zigzag and armchair edges in monolayer graphene nanoribbons. The geometrical edge structure and the number of atomic rows of carbon atoms normal to the ribbon axis determine the electronic structure and ribbon properties (Images courtesy of M. Hofmann, MIT.)

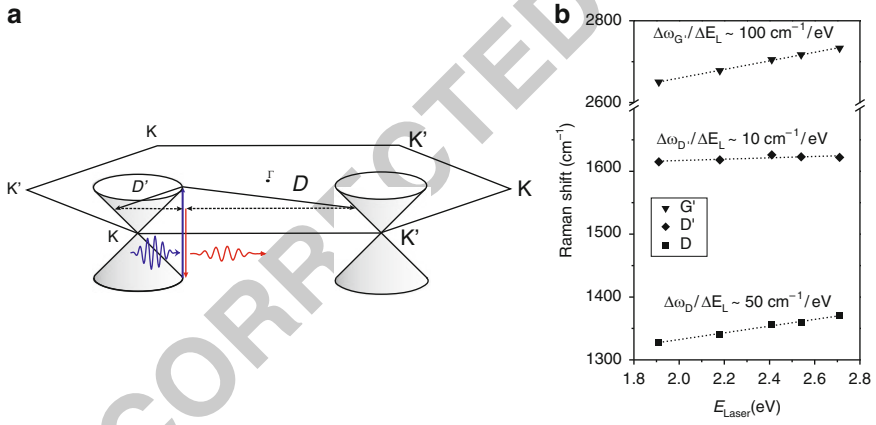

Fig. 2.3 (**a**) Schematics showing the electronic dispersion near the Fermi level at the K and K' points in the hexagonal Brillouin zone of graphene. The light-induced electron–hole formation is indicated by a *gray arrow*. The two resonant electron–phonon scattering processes associated with the D (intervalley) band and the D' (intravalley) band are indicated by *black arrows*. The *dashed arrows* indicate elastic scattering induced by defects. (**b**) Laser energy dependence or dispersion of the frequencies of the D, D', and G' bands which are all dispersive with E_{laser}, but each has a different slope, the smallest slope for the D' band and the largest slope being for the G' band [10]

Defects in the solid are expressed in terms of an impurity potential $V_{\text{imp}}(q)$ which couples two electron wave functions with the wave vector k and $k + q$ to each other. Thus the wave vector k is no longer a good quantum number of an electron, which implies that phonons in the interior of the Brillouin zone ($q \neq 0$) can contribute to the Raman spectra as a higher order Raman process. This is the

UNCORRECTED PROOF

origin of disorder-induced Raman spectra. On the other hand, when we consider the multiple-resonance Raman scattering process, phonons with $q \neq 0$ can be observed without any defect. The intensities of the D band and the D' band $I(\omega, E_{\text{laser}})$ in sp^2 carbons are all enhanced by the double-resonance processes described in Fig. 2.3a [17,23] (the G' band has a similar process). This resonance produces strong coupling between real electronic states. More specifically, when the denominators in the expression for the resonance Raman intensity (or cross section) become small by introducing two real states in the resonance denominators of $I(\omega, E_{\text{laser}})$ which are given in (2.1) [12]:

$$I(\omega, E_{\text{laser}}) = \sum_i \left| \sum_{a,b,c,\omega_{\text{ph}}} \frac{M_{\text{op}}(k, ic) M_{\text{d}}(-q, cb) M_{\text{ep}}(q, ba) M_{\text{op}}(k, ai)}{\Delta E_{ai} (\Delta E_{bi} - \hbar\omega_{\text{ph}})(\Delta E_{ai} - \hbar\omega_{\text{ph}})} \right|^2, \quad (2.1)$$

then the intensity $I(\omega, E_{\text{laser}})$ can become very large. Here ΔE_{ai} in each of the resonance denominators is given by

$$\Delta E_{ai} = (E_{\text{laser}} - (E_a - E_i) - i\gamma_r), \quad (2.2)$$

where γ_r denotes a broadening factor. In (2.1) the subscripts i, a, b, and c, respectively, denote the initial state, the excited state, the first scattered state of an electron by a phonon, and the second scattered state of an electron by a defect. In this double-resonance process, an electron at wave vector k near the K point is first excited to the conduction band state a by a photon absorption process involving the matrix element $M_{\text{op}}(k, ai)$ (see Fig. 2.3 and (2.1)). Next a phonon scatters the electron from a to b with the wave vector q in a crystal momentum-conserving process involving matrix element $M_{\text{ep}}(q, ba)$, after which the electron at b near the K' point in reciprocal space is elastically scattered by a defect back to c near the K point with the wave vector $-q$ by the matrix element $M_{\text{d}}(-q, cb)$. Finally the excited electron emits a photon and returns to the valence band to complete the D-band process, which is seen to include a phonon emission process and an inelastic defect scattering process. The symbols M_{op}, M_{ep} and M_{d} denote the electron–photon, electron–phonon and electron defect scattering matrix elements, respectively. In this double-resonance process, two of three factors in the denominator becomes almost zero (double resonance), which enhances the intensity significantly, resulting in a process with an intensity close to that of a first-order process. The phonon scattering process and the defect scattering process can occur in either order, thereby resulting in a broadening of the Raman linewidth. When these processes are resonant as described above, they enhance the scattering amplitude much more than for nonresonant processes, so that the observed Raman spectra are dominated by the double-resonance D and D'-band scattering processes, both processes fulfilling energy and momentum conservation. Momentum conservation in the presence of disorder can thus be satisfied through an elastic scattering process by a defect, represented by dashed arrows in Fig. 2.3a in addition to the electron–phonon scattering process for the D and D' bands, each of which involves phonons with very different wave vectors, which are known as

UNCORRECTED PROOF

intervalley and intravalley wave vectors, respectively [23]. In contrast, the G' band only involves two-phonon processes with intervalley wave vectors q and $-q$.

In Fig. 2.3b, the dispersions (or slopes) of the frequencies of the D, D', and G' bands are plotted as a function of E_{laser}, whose dependencies are well explained by the double-resonance model [17, 22, 23]. The slope associated with the G' band is about $100\,\text{cm}^{-1}/\text{eV}$ and it is two times larger than the slope of the D band ($50\,\text{cm}^{-1}/\text{eV}$). The D' band also exhibits a weakly dispersive behavior, the slope being $\sim 10\ \text{cm}^{-1}/\text{eV}$ [10].

When we consider the double-resonance Raman scattering processes, the D and D' bands are not the only disorder-induced one-phonon peaks in the Raman spectra for disordered sp^2 materials. Any combination or overtone of the six dispersive phonon energy branches in sp^2 carbons can occur and disorder-induced Raman frequencies can be related to any of the six phonon branches of graphene with the appropriate wave vector which fulfills the double resonance condition and with nonzero electron–phonon matrix elements [17]. The intravalley and intervalley double-resonance processes involve phonons near the Γ and K (or K') points, respectively, and we can vary both the resonant k and q values by changing E_{laser}, as determined by conservation of energy and momentum requirements [23, 27, 28]. Thus by using electronic band structure information, we can determine the phonon dispersion relations around the K and the Γ points, by considering intervalley and intravalley processes, respectively. This approach has been used for obtaining the graphene phonon dispersion relations (see Fig. 2.1b) using Raman spectroscopy [17, 27].

2.1.4 *Concept of the Kohn Anomaly*

The Kohn anomaly refers to the softening of phonon frequencies due to electron–phonon coupling and this effect is very important for describing the G band for graphene and metallic carbon nanotubes. According to this effect, a phonon can bring an electron from the valence band to the conduction band, thus creating an electron–hole pair. This process thus renormalizes the phonon energies and lowers the phonon lifetime [29–32]. This phonon effect is dominant near the Γ and K points of the graphene Brillouin zone, thus generating a highly dispersive phonon branch. These phonons are mainly responsible for the G, G', D, and D' band signals, therefore making the Raman spectra from graphene highly sensitive to this phenomena. Interestingly, the Kohn anomaly effect can be suppressed by changing the Fermi level, since the electrons or holes that are occupied by doping suppress the electron–phonon interaction, causing a strong dependence of the G-band frequency upon doping (see Sect. 16.4 for details).

This effect is specially interesting in carbon nanotubes [33]. The fundamental difference between metallic carbon nanotubes and semiconducting nanotubes is the presence of a band gap in semiconducting nanotubes and the absence of a band gap in metallic nanotubes, as well as the carrier concentration in metallic

UNCORRECTED PROOF

nanotubes at the Fermi energy, leading to a greater importance of the electron–phonon interaction as a phonon scattering process. In practice, the Kohn anomaly is important in modifying the phonon dispersion for metallic nanotubes near the Γ and K (K') points in the Brillouin zone, resulting in both a substantial lowering (by tens of cm^{-1}) of the LO phonon frequency relative to the TO phonon frequency and a broadening in the LO phonon Raman linewidths.

2.1.5 *Introduction to Near-Field Raman Spectroscopy*

Before ending this introductory section, we mention a technique that has strong potential to provide information about local effects in nanostructures, i.e., the near-field technique. Raman spectroscopy will become an even more powerful tool to characterize disorder in sp^2 materials when we learn how to relate specific defects to their corresponding disordering processes and how to obtain quantitative information about the amount of each type of lattice defect. Some important progress has been achieved in this area, as discussed in this chapter, but substantial achievements will come from single-defect spectroscopy. In this sense, near-field Raman spectroscopy is important in providing more spectroscopic information at a smaller length scale Δx than the diffraction limit of $\lambda_{\text{laser}}/2$, where λ_{laser} is the wavelength of the laser. Near-field Raman spectra of sp^2 carbons, such as SWNTs and graphene, have been taken with the help of a sharp tip which enhances the near-field signal [9] and allows detection of localized defects on a length scale of 30 nm when looking at G-band or D-band spectra. Of particular interest would be the study of localized defect features in the vicinity of graphene edges, ion-implanted defects [13], and dopant atom impurities [9]. In the world of sp^2 carbons, near-field Raman spectroscopy has been highly informative for high spatial resolution studies of one-dimensional carbon nanotubes, and high expectations are in place for the use of near-field Raman spectroscopy to study edges and defects in graphene (see further details in Sect. 2.5).

2.2 Characterization of Defects

Accurate defect quantification has been a hard task in the field of sp^2 carbons. To achieve a really accurate quantitative description of defect phenomena, Raman spectroscopy has to be combined with microscopy experiments of the structure. Transmission electron microscopy (TEM) or scanning tunneling microscopy (STM) can characterize structural disorder of the crystal in r-space by probing the local surface density of electronic states, with atomic level resolution. Simultaneous in situ TEM and Raman measurements are, in principle, possible. However, a special experimental setup and special sample preparation methods would be needed for such an experiment. Usually, STM and Raman spectroscopy cannot be easily correlated with each other, since optical spectroscopy probes a volume that is limited

UNCORRECTED PROOF

by the light penetration depth, while STM is mostly sensitive to surfaces. In this context, the possibility of exfoliating graphite to pull out a single graphene sheet provides an ideal situation in which microscopy and spectroscopy can be correlated to probe disorder effects in both r-space and k-space for the same sample. We describe here some early examples of such work.

There are two different major classes of defects in sp^2 carbon systems that have been largely used to study the Raman signature of disorder. One can be said to have point (or zero-dimensional) defects, and this is the case of the point defects produced by ion bombardment. The other system is composed of small graphitic crystallites, where the disorder is actually related mostly to the graphite borders or edges and, therefore, this disorder relates to a one-dimensional defect. This difference in the "dimensionality" of the defect causes differences in the defect behaviors, as discussed below.

2.2.1 Point Defects Induced by Ion Bombardment

There are different ways of introducing point defects in a crystalline lattice, but the use of ion implantation to study defects in graphite is a well-established technique [13]. These experiments are normally carried out as a function of ion dose and for different ion species and different ion energies. Low mass ions at low ion fluence introduce point defects. Increasing the ion dose causes an increasing density of point defects and eventually causes the damaged regions to overlap as discussed for ion-bombarded HOPG and graphene [9, 13, 15, 34, 35]. The work on graphite brings in the complicated aspect of penetration depth and cascade effects. Cascade effects are effects whereby a scattered C atom with a large amount of energy hits another C atom iteratively, similar to the chain reaction of dominoes.

Raman spectroscopy of monolayer graphene, which is intentionally damaged by Ar^+ ion bombardment, was performed in which the energy of ion is kept low to avoid cascade effects[15, 34]. The ion doses range from very low, so that only a few lattice atoms are perturbed, up to ion doses so high as to come close to full disorder. More specifically for Ar^+ ions this corresponds to ion doses varying from 10^{11} to $10^{15} Ar^+/cm^2$, which correspond, respectively, to one defect per 4×10^4 C atoms for the lower limit and to the onset of full disorder in graphene for the upper limit. The defect density in real space was monitored by STM (scanning tunneling microscopy) images which allowed the extraction of the defect density or alternatively values of the average distances between defects [15].

In Fig. 2.4a we show the Raman spectra of a graphene monolayer subjected to different ion bombardment intensities. From Fig. 2.4a it is clear that the Raman spectra for graphene, mildly disordered graphene, and very highly disordered graphene (close to amorphization) are distinctly different from one another. From the pristine sample (bottom spectrum) to the lowest bombardment dose in Fig. 2.4a (10^{11} Ar^+/cm^2), the D-band process is activated, showing a very small intensity relative to the G peak (I_D/I_G). Within the bombardment dose range 10^{11}–10^{13} Ar^+/cm^2,

UNCORRECTED PROOF

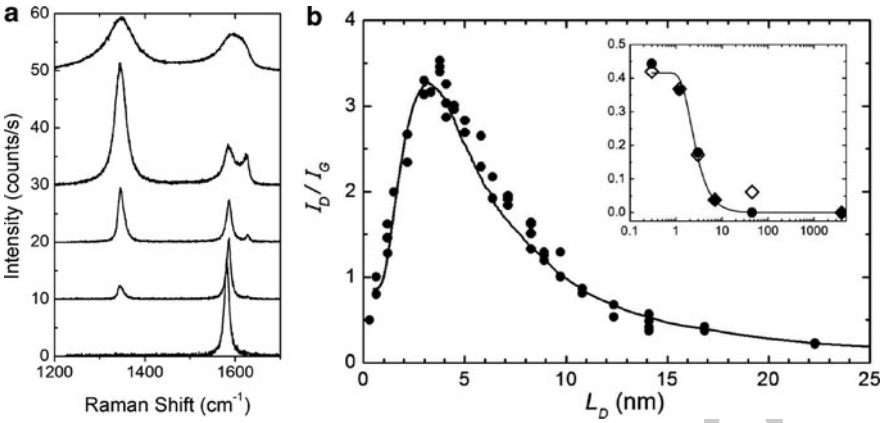

Fig. 2.4 (**a**) Evolution of the first-order Raman spectra (using a $\lambda = 514$ nm laser (2.41 eV)) taken from a graphene monolayer sample deposited on an SiO_2 substrate, subjected to Ar^+ ion bombardment. The ion doses are from the bottom to the top, 10^{10}, 10^{11}, 10^{12}, 10^{13}, and 10^{14} Ar^+/cm^2 [15]. (**b**) The I_D/I_G data points from three different monolayer graphene samples as a function of the average distance L_D between defects. The *solid line* is a modeling of the experimental data using (2.3). The *inset* shows a plot of I_D/I_G vs. L_D on a log scale for L_D for two samples: (i) *open points* for a ~50-layer graphene sample and *solid circles* are for a small piece of HOPG near a graphene piece. (ii) *solid diamond points*, for a 2 mm-thick bulk HOPG sample, whose measured values are here scaled by $(I_D/I_G) \times 3.5$ [15]

UNCORRECTED PRC

the intensities of the disorder-induced peaks increase in intensity. The second disorder-induced peak around ~1,620 cm^{-1} (the D′ band) also becomes evident within this bombardment dose range. However, above 10^{13} Ar^+/cm^2, the graphene Raman spectra start to broaden significantly and end up exhibiting a profile similar to the graphene phonon density of states (PDOS) for the highest ion dose of 10^{15} Ar^+/cm^2 [15].

In Fig. 2.4b we plot the I_D/I_G as a function of the average distance between defects L_D, in which we can quantify the degree of disorder. As seen in this figure, the I_D/I_G ratio has a nonmonotonic dependence on L_D, increasing initially with increasing L_D up to $L_D \sim 3.5$ nm, where I_D/I_G in Fig. 2.4b has a peak value, and then decreasing for $L_D > 3.5$ nm. Such a behavior suggests the existence of two disorder-induced competing mechanisms contributing to the Raman D-band intensity, which we describe next.

2.2.2 *Model for the D-Band Activated Region*

To explain the I_D/I_G dependence on L_D, we propose the so-called D-band activation model which is illustrated in Fig. 2.5 [15]. This model assumes that a single impact of an ion on the graphene sheet causes modifications on two length scales, here denoted by r_A and r_S (with $r_A > r_S$), which are, respectively, the radii

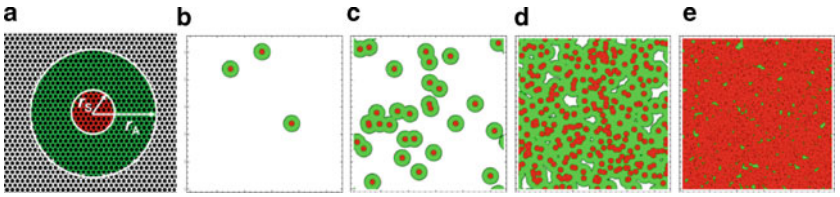

Fig. 2.5 (**a**) Definition of the "activated D'" A-region (*darkest gray*) and "structurally disordered D'" S-region (*dark gray*). The radii are measured from the ion impact point which is chosen randomly in our simulation. (**b–e**) shows 55 nm×55 nm portions of the graphene simulation cell, with snapshots of the structural evolution of the graphene sheet for different defect concentrations: (**b**) 10^{11} Ar^+/cm^2; (**c**) 10^{12} Ar^+/cm^2; (**d**) 10^{13} Ar^+/cm^2; (**e**) 10^{14} Ar^+/cm^2, like the five spectra in Fig. 2.4a [15]

of two circular areas measured from the ion impact point (see Fig. 2.5). Within the shorter radius r_S, a structurally disordered S-region occurs relative to the point of impact. For distances larger than r_S but shorter than r_A, the lattice structure is preserved, but the Raman D band is activated. We call this the activated or A-region. In qualitative terms, an electron–hole excitation will only be able to "see" the structural defect if the electron–hole pair is created sufficiently close to the defect site and if the excited electron (or hole) lives long enough for the defective region to be probed by Raman spectroscopy.

For understanding this model, stochastic simulations were performed for each disorder levels [15]. Snapshots of each disorder concentration are shown in Fig. 2.5b–e for the same argon ion concentrations as in Fig. 2.4a. In the stochastic simulations of the bombardment process, we randomly chose the impact points for the ions, combined with (2.3) and select the parameters $r_A = 3\,\text{nm}$ and $r_S = 1\,\text{nm}$, which give the full line curve in Fig. 2.4b. The calculated result is in excellent agreement with the experimental results (points) in this figure [15]. The length scale $r_S = 1\,\text{nm}$, which defines the structurally disordered area, is in excellent agreement with the average size of the disordered structures seen in the STM images. This parameter should, however, not be universal, but it should be specific to the bombardment process, the ion bombardment conditions, and the specific ions used for the ion bombardment. The Raman relaxation length ℓ for the defect-induced resonant Raman scattering in graphene for $E_{\text{laser}} = 2.41\,\text{eV}$ (514 nm) is found to be $\ell = r_A - r_S = 2\,\text{nm}$. It is impressive how short this relaxation length is for this type of point defect.

It is important to have an equation relating I_D/I_G to L_D. Such an equation can be obtained by solving the rate equations for the bombardment process. The entire regime ($0 < L_D < \infty$) can be fitted using

$$\frac{I_D}{I_G} = C_A \frac{r_A^2 - r_S^2}{r_A^2 - 2r_S^2}\left[\exp\left(\frac{-\pi r_S^2}{L_D^2}\right) - \exp\left(\frac{-\pi(r_A^2 - r_S^2)}{L_D^2}\right)\right] + C_S\left[1 - \left(\frac{-\pi r_S^2}{L_D^2}\right)\right], \tag{2.3}$$

UNCORRECTED PROOF

where the fitted parameters are $C_A = (4.2 \pm 0.1)$, $C_S = (0.87 \pm 0.05)$, $r_A = (3.00 \pm 0.03)$ nm and $r_S = (1.00 \pm 0.04)$ nm [15]. The C_A parameter is a measure of the maximum possible value of the I_D/I_G ratio in graphene, which would occur in a hypothetical situation in which K–K′ wave vector mixing would be allowed everywhere, but no damage would be made to the hexagonal network of carbon atoms. C_A should then be defined by the electron–phonon matrix elements, and the value $C_A = 4.2$ is then in rough agreement with the ratio between the electron–phonon coupling for the iTO phonons evaluated between the Γ and K points in the Brillouin zone [36]. The C_S parameter is then the value of the I_D/I_G ratio in the highly disordered limit, which has not yet been addressed theoretically. For large values of L_D ($L_D > 6$ nm), a much simpler formula can be used, i.e., $I_D/I_G = A/L_D^2$, where $A = (102 \pm 2)$ nm^2.

This model has been extended to account also for the evolution of the D'- and G'-band intensities. Ferreira et al. [34] also described carefully the evolution of the frequencies, intensities, and full-width at half maximum intensity for all the observed peaks in the Raman spectra of graphene, as a function of ion induced disordering and the number of graphene layers.

2.2.3 Line Defects at the Edges of Nanographene

Now we turn into the other class of defects, i.e., the one-dimensional defects represented by the graphene borders or edges. By scanning the focused laser light of an optical microscope on a graphite nanocrystallite or graphene, we can observe Raman signals as a function of position, which is known as confocal Raman imaging. The G-band intensity is uniform over the whole graphene surface, while the D-band intensity is localized where the crystalline structure is not perfect, mostly at the edges of the crystallite. We therefore expect to see elastic scattering events at the edges which contribute to the D-band intensity [37–39]. Notice also that the D-band intensity varies from edge to edge, and this D-band intensity is dependent on the light polarization direction and the atomic structure at the edge, as discussed later.

As pointed in the introduction, the intensity ratio of the D band to the G band, I_D/I_G, is frequently used for the evaluation of crystallite dimensions L_a [3]. The model described for point defects in Sect. 2.2.2 also applies to the edges after several additional effects are taken into account [9]. When we consider a square of crystallite size L_a, the intensity of the G band will vary as $I_G \propto L_a^2$. The intensity of the D band will, however, depend on the width δ of the "border" (of around 2–3 nm) where the D band is activated and is given by $I_D \propto L_a^2 - (L_a - 2\delta)^2$ consistent with the findings in Sect. 2.2.2. The intensity ratio will then be given by

$$\frac{I_D}{I_G} = \alpha \left[4 \left(\frac{\delta}{L_a} - \frac{\delta^2}{L_a^2} \right) \right], \tag{2.4}$$

where the scaling factor α is dependent on the appropriate matrix elements [9].

UNCORRECTED PROOF

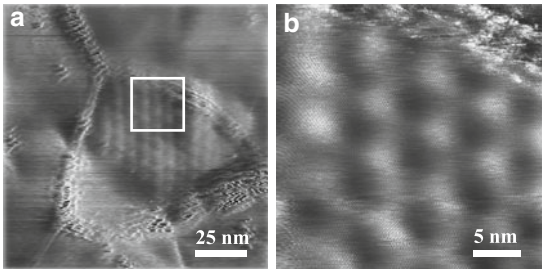

Fig. 2.6 Scanning tunneling microscopy (STM) images with atomic resolution obtained from the surface of a nanographite crystallite of a sample with $L_a = 65$ nm. (**a**) A Moire pattern at the crystallite surface is observed. (**b**) Magnification of the region delineated by the *white square* in part (**a**) [40]

When we take a limit $L_a \gg \delta$, where the crystallite size is large compared to the heavy damage range, (2.4) can be simplified to yield the Tuinstra–Koenig relation [3]

$$\frac{I_D}{I_G} = C(E_{\text{laser}})/L_a, \tag{2.5}$$

in which the value of the empirical constant $C(E_{\text{laser}})$ depends on E_{laser}. One could then expect that, once the relaxation length and matrix element ratio were measured for the D-band scattering in ion-bombarded graphene (Sect. 2.2.2), these values could just be used to obtain α and δ. However, the relaxation length and matrix element ratio depend on the structurally disordered area (S_S) shown in Fig. 2.5, which is not well defined for nano-graphite. Figure 2.6 shows two scanning tunneling microscopy (STM) images with atomic resolution obtained from the surface of a crystallite in a nanographite sample with $L_a = 65$ nm. The atomic arrangement of the carbon atoms observed in these images indicates that the samples are formed by nanographitic crystallites, with a disordered grain boundary between crystallites [40]. Variability associated with grain boundaries such as in Fig. 2.6 may also be responsible for the different I_D/I_G vs. L_a results obtained by different groups, as reported in the literature. However, I_D/I_G also depends on E_{laser}, the laser excitation energy.

This important fact that the constant $C(E_{\text{laser}})$ depends on E_{laser} is known since 1984 [14], but $C(E_{\text{laser}})$ has been quantitatively determined only more recently [41], using experimental results from nanographites with different L_a values prepared from diamond-like carbon (DLC) films heat treated at different temperatures T_{htt} [41]. In Fig. 2.7a Raman spectra for the $T_{\text{htt}} = 2{,}000$°C sample ($L_a = 35$ nm) for five different E_{laser} values are shown. The spectra are normalized to the G-band intensity, and clearly the ratio (I_D/I_G) increases with decreasing E_{laser}. To clarify this point, we show in Fig. 2.7b, the Raman spectra for different crystallite sizes L_a using the same excitation laser energy $E_{\text{laser}} = 1.92$ eV [41], where the L_a sizes were determined by using both STM and X-ray measurements. These L_a values were thus correlated with the I_D/I_G intensity ratios measured at different laser energies leading to a general equation for determining L_a as a function of both the laser excitation energy and the (I_D/I_G) intensity ratio [41].

UNCORRECTED PROOF

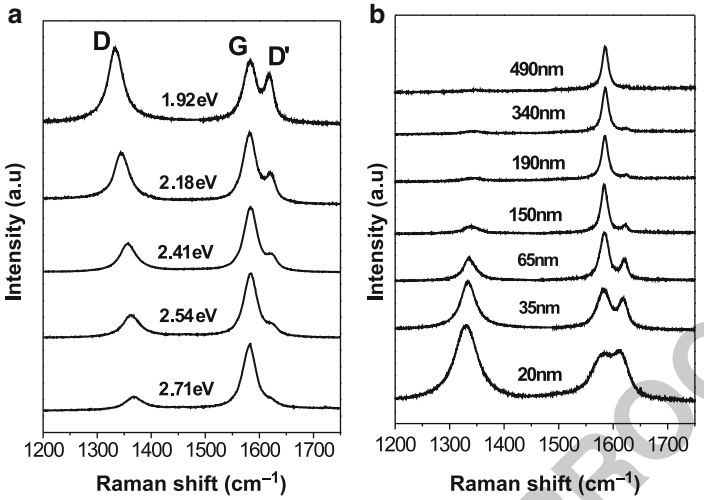

Fig. 2.7 The first-order Raman spectra of (**a**) a nanographite sample heat treated at 2,000°C (L_a = 35 nm), for five different laser excitation energies (1.92 eV, 2.18 eV, 2.41 eV, 2.54 eV, and 2.71 eV). (**b**) Nanographite samples with different crystallite sizes L_a using 1.92 eV laser excitation energy [41]

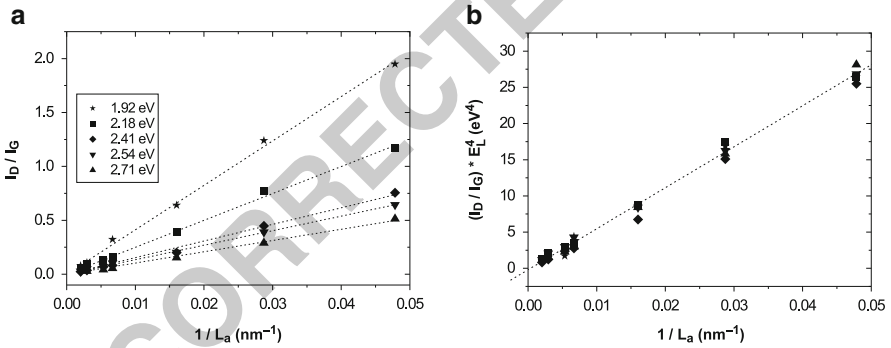

Fig. 2.8 (**a**) The intensity ratio I_D/I_G for nanographite samples is plotted vs. $1/L_a$ using five different laser excitation energies (see text). (**b**) All curves shown in part (**a**) collapse onto the same curve in the $(I_D/I_G)E_L^4$ vs. $(1/L_a)$ plot where E_L denotes the laser excitation energy [41]

UNCORRECTED PROOF

Figure 2.8a shows a plot of (I_D/I_G) vs. $1/L_a$ for all samples shown in Fig. 2.7. It is clear in Fig. 2.8b that I_D/I_G for a given sample can be scaled by E_{laser} as $(I_D/I_G)E_{laser}^4$ vs. L_a. From this relation we can estimate L_a using any laser line in the visible range [41]:

$$L_a(\text{nm}) = \frac{560}{E_{laser}^4}\left(\frac{I_D}{I_G}\right)^{-1} = (2.4\times10^{-10})\lambda_{laser}^4\left(\frac{I_D}{I_G}\right)^{-1}, \qquad (2.6)$$

where the laser excitation is given in terms of both E_{laser} (eV) and the corresponding wavelength λ_{laser} (nm). This behavior is consistent with D-band intensity calculations [37]. A similar analysis has also been made for carbon foams [42]. In the literature, the (I_D/I_G) ratio is often reported at 2.41 eV, where the I_D/I_G ratio is relatively low.

2.3 Characterization of Edges

As discussed in Sect. 2.1.2, finite size graphene can have two symmetric edge structures which are known as zigzag and armchair edges [43]. Unlike single wall carbon nanotubes where no edge structures exist along the walls of the nanotubes, experiments show that armchair and zigzag edges of heat-treated graphene nanoribbons are stable and dominant. Here we discuss how to characterize the edge structures of graphene by Raman spectroscopy.

2.3.1 Overview of Graphene Edges

The electron and phonon states exhibit edge-specific properties for armchair or zigzag edges of graphene nanoribbons which can be observed by Raman spectroscopy. A graphene nanoribbon is defined as a one-dimensional graphene strip with edges at both sides and with a fixed width whose structure is specified by a vector in the direction of the ribbon width, similar to the chiral vector of single wall carbon nanotubes [43, 44]. A graphene nanoribbon is obtained either by (1) unrolling nanotubes by heating [14, 15], (2) by cutting a graphene sheet by electron-beam lithography [47], or by (3) heating nanodiamond [25, 48].

In the case of the zigzag edge, localized electron states which are called edge states appear and form a flat energy band at the Fermi energy from the K point to the M point in the two-dimensional Brillouin zone [43, 44]. Since the edge states are partially occupied by π electrons, the magnetic properties of edge states show ferromagnetic behavior because of the exchange interaction between spins in the flat energy band structure [49]. Another important fact about the edge state is that the amplitude of the wave function has a large value only on one of the two sublattices of graphene. This fact enhances the electron–phonon interaction [50, 51] only near the zigzag edge. The fact that the wave function has a large value only on one sublattice corresponds to the pseudospin polarized state of graphene [51]. Here the pseudospin of graphene is defined by the two component wave function of π electrons [52]. Using this fact, possible superconductivity may appear at these edges [53, 54]. Igami et al. discussed the possible phonon edge states of graphene nanoribbons with zigzag edges [55]. Similar edge phonon modes are observed at the tube edges in a single wall carbon nanotube (SWNT) with finite length [56].

UNCORRECTED PROOF

For the armchair edges of nanoribbons, double-resonance theory (see Sect. 2.1.3) tells us that the D band is strong for the armchair edges since the scattering at the armchair edge corresponds to the intervalley scattering which is relevant to the D-band Raman intensity, while the scattering at the zigzag edge corresponds to intravalley scattering and is very weak [39]. Further, edge-localized phonon modes are observed for thin graphene nanoribbons [57]. Combined with the phonon-softening phenomena of the G band (see Sect. 16.4), the polarization dependence of the Raman signal characterizes the signal of the LO and TO phonon modes for the G band [58], and we can use these polarization techniques to characterize and to distinguish between the different edge structures by Raman spectroscopy. Hereafter we discuss each subject one by one.

2.3.2 *The Characterization of Graphene Edges from Their D-Band Scattering*

In nanographitic samples formed by aggregates of small crystallites, the crystallite borders form defects in real space. Since the crystallites have different sizes and their boundaries are randomly oriented, the defect wave vectors exhibit all possible directions and values. Therefore, the existence of a defect with momentum exactly opposite to the phonon momentum is always possible, giving rise to double-resonance processes [17, 22] connecting any pair of points (electron wave vectors) around the K and K' points in the first Brillouin zone of graphite or graphene. In this case, the intensity of the D band is isotropic and does not depend on the light polarization direction. However, in the case of edges, the D-band intensity is anisotropic because the double-resonance process cannot occur for any arbitrary pair of k points [39]. Since, in real space, the edge defect is well localized in the direction perpendicular to the edge, it is completely delocalized in this direction in reciprocal space and, therefore, the wave vector of such a defect assumes all possible values perpendicular to the edge. Hence, the defect associated with an edge has a one-dimensional character and it is only able to transfer momentum in the direction perpendicular to the edge.

Here we show that the disorder-induced D band obtained from graphene edges provides useful information about the atomic structure of these edges. The D-band scattering is strongly anisotropic and depends on the orientation of the carbon hexagons with respect to the edge, in the armchair or zigzag arrangements [39]. This anisotropy can be used to define the local degree of order of the atomic structure at the edge. The physics leading to this structurally selective effect is explained on the basis of the well-established double-resonance effect [17, 22] applied to a semi-infinite crystal bounded by a one-dimensional defect.

In Fig. 2.9a, we show three Raman spectra at three different regions of a highly oriented pyrolytic graphite (HOPG) [39]. The inset to Fig. 2.9a shows a high-resolution STM (scanning tunneling microscopy) image of the sample. Further details about the STM technique can be found in Chap. 3. Regions 1 and 2 are at

UNCORRECTED PROOF

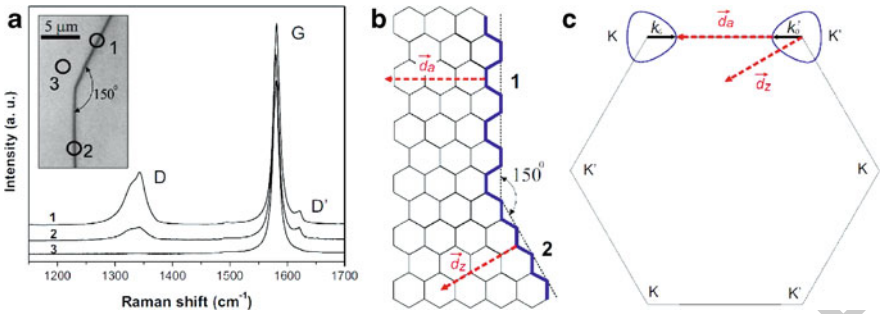

Fig. 2.9 (**a**) Raman spectra at different regions of a highly oriented pyrolytic graphite (HOPG). The *inset* shows an optical image of the sample. Regions 1 and 2 are at HOPG edges, while region 3 is on the flat HOPG surface. (**b**) Idealized structure of the edges shown at the *inset* to part (**a**). The *bold lines* highlight the edge structures, armchair for edge 1 and zigzag for edge 2. The wave vectors of the defects associated with these edges are represented by $\boldsymbol{d}_a$ for armchair and $\boldsymbol{d}_z$ for the zigzag edges. (**c**) The first Brillouin zone of graphene oriented according to the lattice in the real space shown in part (**b**). Note that only the armchair $\boldsymbol{d}_a$ vector is able to connect points belonging to equienergy contours surrounding two inequivalent K and K' points (Adapted from Ref. [39].)

UNCORRECTED PROOF

HOPG step edges, while region 3 is taken at an interior point of the HOPG sample. In all spectra, the light propagation is perpendicular to the HOPG basal plane and the polarization of the incident light is parallel to the edge direction in spectra 1 and 2. The G band (centered at approximately 1,580 cm^{-1}) is present in all spectra with the same intensity. The Raman features at approximately 1,340 and 1,620 cm^{-1} are the disorder-induced D and D' bands, respectively. The disorder-induced D and D' bands are observed in spectra 1 and 2, but not in spectrum 3, since spectrum 3 was taken at an interior region of the HOPG with a crystalline order (see inset to Fig. 2.9a). As shown in Fig. 2.9a, the D band is about four times less intense in spectrum 2 compared to spectrum 1, whereas the D'-band intensity remains almost constant for both spectra. The different intensities observed for the D band in spectra 1 and 2 indicate that the the D-band intensity is coming from graphite edges.

The STM images of the edges revealed that edge 1 shown in Fig. 2.9a has an armchair structure, whereas edge 2 has a zigzag structure. To clarify this picture, Fig. 2.9b shows the idealized structure of the edges. The bold blue lines highlight the edge structures, armchair for edge 1 and zigzag for edge 2. The wave vectors of the defects associated with these edges are represented by $\boldsymbol{d}_a$ for armchair and $\boldsymbol{d}_z$ for the zigzag edge. Figure 2.9c shows the first Brillouin zone of graphene oriented according to the lattice in the real space shown in Fig. 2.9b. Note that only the armchair $\boldsymbol{d}_a$ vector is able to connect points belonging to equienergy contours surrounding two inequivalent K and K' points. An important fact is the change of the wave vector by scattering at the zigzag edges d_z does not connect K and K' points but connects K and K or $K'$and K', which means intravalley scattering. This means that the intervalley double-resonance process associated with this defect cannot occur for a zigzag edge, thereby explaining why the D band is much less intense

in the spectra obtained in zigzag edge 2. On the other hand, the D' band is given by an intravalley process, which connects points belonging to the same equienergy contour around the K (or K') point [17]. In this case, momentum conservation can be satisfied by both $\boldsymbol{d}_a$ and $\boldsymbol{d}_z$ vectors[3] and, therefore, the observation of the D' band must be independent of the edge structure though the relative intensity might be different. This conclusion is confirmed by the experimental result shown in Fig. 2.9a, where the D′ band has a similar intensity in both spectra 1 and 2, with armchair and zigzag structures, respectively. It is important to note the observation of a weak D band in spectrum 2, where it should be absent. This weak D band is related to the actual atomic structure of the edge, allowing the scattering of the electron by phonons and defects with wave vectors not perpendicular to the edge. Similar measurements performed on different closely related armchair and zigzag graphene edges show different D-band intensity ratios, indicating different degrees of order for the local atomic arrangement at the different edges [59–61].

We now turn our attention to the dependence of the D-band scattering intensity on the polarization of the incident light relative to the edge direction. Figure 2.10a shows the topographic image of a single graphene layer on a glass substrate [40]. Figure 2.10b–d shows the corresponding Raman intensity images showing the G, G' and D-band intensities, respectively. Notice that the G-band intensity is roughly uniform along the graphene surface. A similar situation occurs for the G' band, which is the overtone of the D band but does not require a disorder-induced process to become Raman active, since momentum conservation is guaranteed in two-phonon Raman processes occuring for the G' band [62]. On the other hand, the D band can be detected only near the graphene edges. Figure 2.10e shows Raman scattering spectra acquired at two different locations (indicated in Fig. 2.10a). The upper spectrum was acquired near the edge of the graphene layer whereas the lower spectrum was recorded $\approx 1\,\mu$m from the edge. The D band appears only in the spectrum acquired near the edge, indicating that the graphene sheet is essentially free of structural defects. The Raman scattering spectra also reveal that the G' band is composed of a single peak, which confirms that the sample is a *single* graphene sheet [63]. All confocal Raman images shown in Fig. 2.10b–d were recorded with the polarization vector $\boldsymbol{P}$ of the excitation laser beam oriented parallel to the graphene edge (y direction in Fig. 2.10b). Notice that the D-band intensity associated with the top edge in Fig. 2.10d is weaker than that obtained from the side edges, as we explain below.

In 2003, Grüneis et al. predicted an anisotropy in the optical absorption coefficient of graphene given by $W_{\text{abs}} \propto |\boldsymbol{P} \times \boldsymbol{k}|^2$, where $\boldsymbol{P}$ is the polarization of the incident (scattered) light for the absorption process, and $\boldsymbol{k}$ is the wave vector of the electron measured from the K or K' point [64]. The thickness of the gray region around the K and K' points at the corners of the first Brillouin zone of graphene shown in Fig. 2.10g illustrates this anisotropy in the optical absorption relative to $\boldsymbol{P}$. Note that the light absorption has a maximum efficiency for electrons

[3] It is noted that $\boldsymbol{d}_a$ connects two k points on a constant energy contour.

UNCORRECTED PROOF

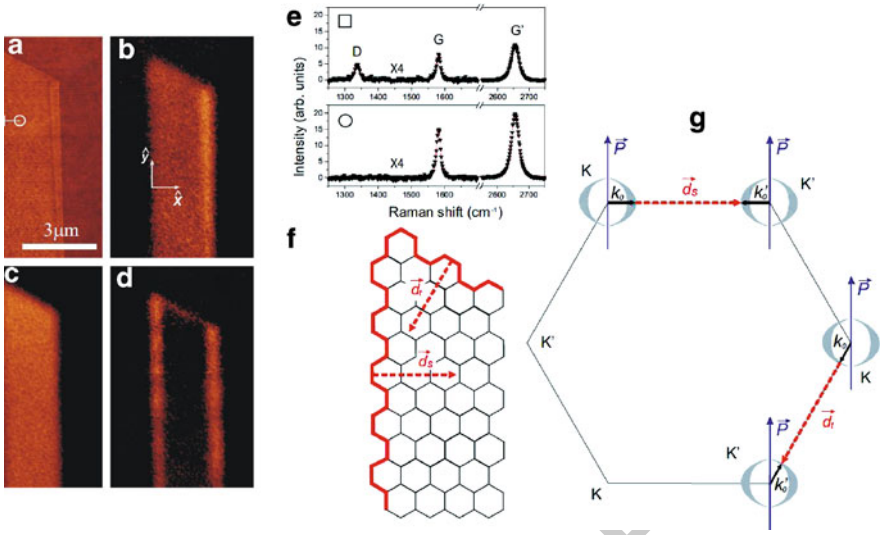

Fig. 2.10 (**a**) Topographic image of a single graphene layer on a glass substrate. (**b**)–(**d**) Corresponding Raman intensity images showing the G-, G'- and D-band intensities, respectively. (**e**) Raman scattering spectra acquired at two different locations of the graphene layer shown in part (**a**). The upper spectrum was acquired near the edge of the graphene layer [position indicated by the *white square* in panel (**a**)] whereas the lower spectrum was recorded $\approx 1\,\mu$m from the edge [position indicated by the *white circle* in panel (**a**)]. (**f**) The idealized structure of the edges of the graphene layer shown in panel (**a**). The wave vectors of the defects associated with these edges are represented by $\boldsymbol{d}_s$ for the left side edge and $\boldsymbol{d}_t$ for the top edge. Notice that both edges have the same symmetry, which based on the strong D-band scattering intensity from the side edges, we suppose to be armchair. (**g**) The first Brillouin zone of graphene oriented according to the lattice in real space shown in part (**f**). $\boldsymbol{P}$ is the polarization vector of the incident light according to the experiment that is responsible for the images shown in parts (**b**)–(**d**). The thickness of the gray region around the K and K' points illustrates the anisotropy in the optical absorption relative to $\boldsymbol{P}$. Note that the light absorption (emission) has a maximum for electrons with wave vectors perpendicular to $\boldsymbol{P}$, and it is null for electrons with wave vectors parallel to $\boldsymbol{P}$ (Adapted from [40].)

UNCORRECTED

with wave vectors perpendicular to $\boldsymbol{P}$, and the efficiency is null for electrons with wave vectors parallel to $\boldsymbol{P}$. A singularity in the density of phonons that participates in the one-dimensional double-resonance intervalley process gives rise to the D band. This singularity in the phonon density of states [64] restricts the wave vector of the electron to the direction perpendicular to the armchair edge ($\boldsymbol{k}_0$ and $\boldsymbol{k}'_0$ in Fig. 2.10g). However, as pointed out before, such electrons will only absorb light efficiently if the polarization vector of the incident light is perpendicular to the electron wave vector, and therefore a strong double-resonance process will occur only if the polarization vector of the incident light is parallel to the edge. As shown in Fig. 2.10g, this is the case for D-band scattering that originates from the side edges of the graphene piece shown in Fig. 2.10a, which generate defects whose wave vector $\boldsymbol{d}_S$ (see Fig. 2.10f) connects electron wave vectors $\boldsymbol{k}_0$ and $\boldsymbol{k}'_0$ that are located at maxima in the light absorption efficiency around the K and K' points,

respectively. On the other hand, the top edge in Fig. 2.10a generates defects whose wave vectors $\boldsymbol{d}_t$ (see Fig. 2.10f) connect electron wave vectors $\boldsymbol{k}_0$ and $\boldsymbol{k}'_0$ which are located near nodes in the light absorption efficiency around the K and K' points, respectively (see Fig. 2.10g). This is the reason why the intensity of the D-band signal obtained from the top edge in Fig. 2.10d (forming a relative angle of $\sim 60°$ with $\boldsymbol{P}$) is weaker than that obtained from the side edges. Notice that if the incident light polarization vector is perpendicular to the edge, the D-band Raman scattering cannot be observed even for armchair edges [39, 59, 60].

2.3.3 *Polarization Dependence of the Raman Spectra at Edges*

Next we discuss Raman-active phonon modes of graphene edges within non-resonance Raman theory [65]. In the case of graphene, since we always satisfy the resonance condition for Raman spectra, the relative Raman intensity is directly determined by the Raman tensor. Thus a nonresonance Raman calculation can give reasonably reliable information. In Fig. 2.11, we show the unit cell of a graphene ribbon with (a) armchair and (b) zigzag edges. The graphene ribbons lie in the xy plane in which the edges (or the 1D periodicity direction) lie along the x direction. The direction of the incident and scattered light is selected as the z (y) direction for the XX, XY, and YY (ZZ) polarizations. Here we should mention that the in-plane and out-of-plane bond polarizabilities need not be the same, which has been shown for boron nitride BN [66]. Thus we cannot always compare the Raman intensity for ZZ and the in-plane polarization, but we can discuss the relative intensity within the ZZ configuration.

The ribbon width N is defined from the number of C–C lines parallel to the ribbon direction, and the corresponding numbers of carbon atoms in the unit cell of

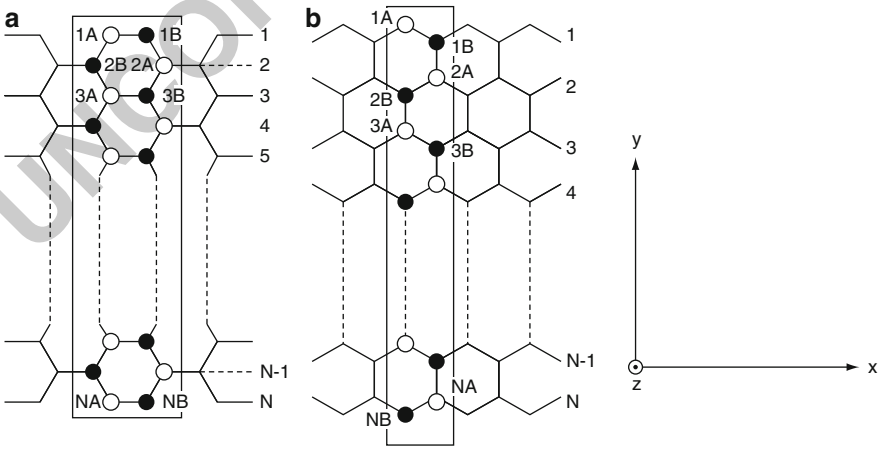

Fig. 2.11 The unit cell of an (**a**) armchair and (**b**) zigzag nanoribbon. The graphene ribbon lies in xy plane and the edge (periodic) direction is along x [65]

UNCORRECTED PROOF

the armchair and zigzag nanoribbons are $2N$ for both cases (see Fig. 2.11). Here, we consider, for simplicity, only N = odd for armchair (zigzag) nanoribbons in which the corresponding point group symmetry is D_{2h} (C_{2v}). The case N = even for armchair (zigzag) nanoribbons corresponds to C_{2v} (D_{2h}) symmetry. Further, in the special case of the zigzag nanoribbons with N = half integer, a different type of edge (the so-called the Klein edge) appears [49]. As far as we discuss edge phonons, we did not find any odd–even dependence of N on the phonon properties.

The scattering geometry is specified by the symbols $iISs$ ($i, s = x, y, z$ and $I, S = X, Y, Z$) in which i and s (I and S) denote propagating (polarization) directions of the incident and scattered light, respectively. In bond polarization theory, we cannot specify the propagating direction but we can only specify the polarization direction, because the electromagnetic wave propagations i and I (or s and S) should be perpendicular to each other. Here we consider the following four back-scattering geometries $zXX\bar{z}$, $zXY\bar{z}$, $zYY\bar{z}$, and $yZZ\bar{y}$ in which the overlines $\bar{z}$ and $\bar{y}$ refer to the negative z and negative y directions, respectively.

The Raman-active modes belong to irreducible representations of D_{2h} point group: (A_g, x^2, y^2, z^2), (B_{1g}, xy), (B_{2g}, xz), and (B_{3g}, yz); C_{2v}: (A_1, x^2, y^2, z^2), (A_2, xy), (B_1, xz), (B_2, yz). In particular, for the scattering geometries $zXX\bar{z}$ and $zYY\bar{z}$, the A_g (A_1) mode is Raman active, while for $zXY\bar{z}$ and $zYX\bar{z}$, the B_{1g} (A_2) mode is Raman active for D_{2h} (C_{2v}).

In Fig. 2.12, calculated results of the Raman spectra are shown for four different geometries of the polarization directions. Here RBLM (RBLM3), EDGE, LO and TO denote, respectively, the radial breathing-like phonon mode (its third overtone),

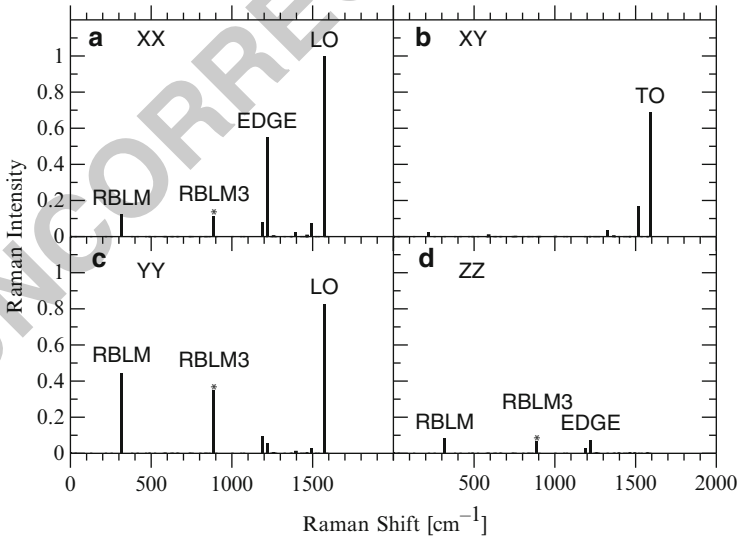

Fig. 2.12 The nonresonance Raman spectra of an $N = 9$ armchair nanoribbon for the scattering geometries of (**a**) $zXX\bar{z}$, (**b**) $zXY\bar{z}$, (**c**) $zYY\bar{z}$, and (**d**) $yZZ\bar{y}$. The Raman intensity is normalized to the one for the largest Raman signal for the four geometries shown [65]

UNCORRECTED PROOF

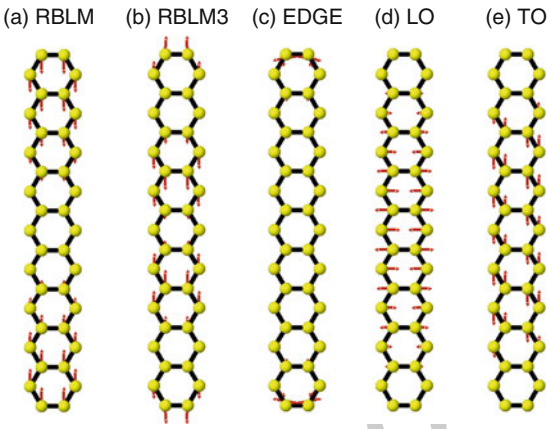

Fig. 2.13 Phonon eigenvectors of an $N = 19$ armchair nanoribbon for (**a**) RBLM, (**b**) RBLM3, (**c**) EDGE (**d**) LO, and (**e**) TO phonon modes [65]

the edge phonon modes, the longitudinal optical and the in-plane transverse optical phonon modes, whose vibration amplitudes are illustrated in Fig. 2.13. It is noted that the out-of-plane optical phonon mode is not a Raman-active mode. The LO, RBLM (RBM3), and edge modes belong to A_g symmetry, while the TO belongs to B_{1g} (xy) symmetry, which are all Raman active. The TO and LO modes are related to the Raman G band of sp^2 carbon materials whose vibrational amplitudes are perpendicular and parallel, respectively, to the armchair edge and are homogeneous in the interior region of the nanoribbon. In the RBLM, the ribbon width is vibrating, which is similar to the radial breathing mode of a single wall carbon nanotube [67]. The RBLM appears at relatively lower (300cm^{-1}) frequency regions and the frequency is inversely proportional to the ribbon width. In the experimental situation, the observation of the RBLM is possible only when a fixed ribbon width is made. Further we should consider the interaction of the nano ribbon with the substrate which modifies the RBLM frequency.

The frequencies of the edge phonon modes are around $1{,}250\text{cm}^{-1}$ if we used the force constant set for sp^2 carbon. However, around the armchair edges without any termination, the C–C bond at the edge becomes triple bonds and thus the calculated edge phonon frequency by first principles calculations becomes relatively high (around $2{,}200\,\text{cm}^{-1}$). When the dangling bond is terminated by H atoms, then the edge phonon modes of armchair edges are downshifted to $1{,}530\,\text{cm}^{-1}$, which is consistent with the recent Raman measurements on very thin nanographene ribbons[57]. The amplitude of the edge phonon mode is localized only near the armchair edge and its vibrating direction is parallel to the edge. Thus, the Raman intensity for the edge mode is large for the XX polarization geometry compared with the YY geometry. The TO phonon modes have a large Raman intensity for the XY geometry since TO belongs to B_{1g}. RBLM has a significant Raman intensity for all XX, YY, and ZZ geometries which are common to A_g symmetry modes [67, 68].

UNCORRECTED PRO

In the ZZ geometry, the G-band modes (TO and LO) disappear and only weak signals of RBLM (RBLM3) and edge phonon modes can be seen. A relatively strong peak at 889 cm^{-1}, which can be seen also in the XX and YY geometries, belongs to a higher frequency RBLM with three nodes of vibration (RBLM3). Although the wavelength of the three node mode is one third of the fundamental RBLM (317 cm^{-1}), the corresponding phonon frequency (880 cm^{-1}) is slightly smaller than three times RBLM. This is because the longitudinal acoustic phonon energy dispersion deviates from a linear energy dispersion near the zone boundary region of the Brillouin zone.

In Fig. 2.14, the Raman intensity for an $N = 9$ zigzag nanoribbon is plotted for the scattering geometries of (a) $zXX\bar{z}$, (b) $zXY\bar{z}$, (c) $zYY\bar{z}$, and (d) $yZZ\bar{y}$. The Raman signal for the ZZ geometry is 10 times enlarged relative to that for the XX, XY, and YY geometries. The vibrational directions of the RBLM, RBLM3, EDGE, TO, and LO phonon modes are illustrated in Fig. 2.15. In the case of zigzag nanotubes, the TO, RBLM (RBLM3), and edge modes belong to A_1 symmetry while the LO mode belongs to A_2 symmetry. Thus the TO, RBLM, (RBLM3) and edge phonon modes can be seen in the XX, YY, and ZZ geometries, while the LO phonon mode can be seen in the XY geometry. Generally we cannot distinguish between LO and TO phonon modes from these experiments. However, we will show in the following section that only LO phonon modes show phonon-softening

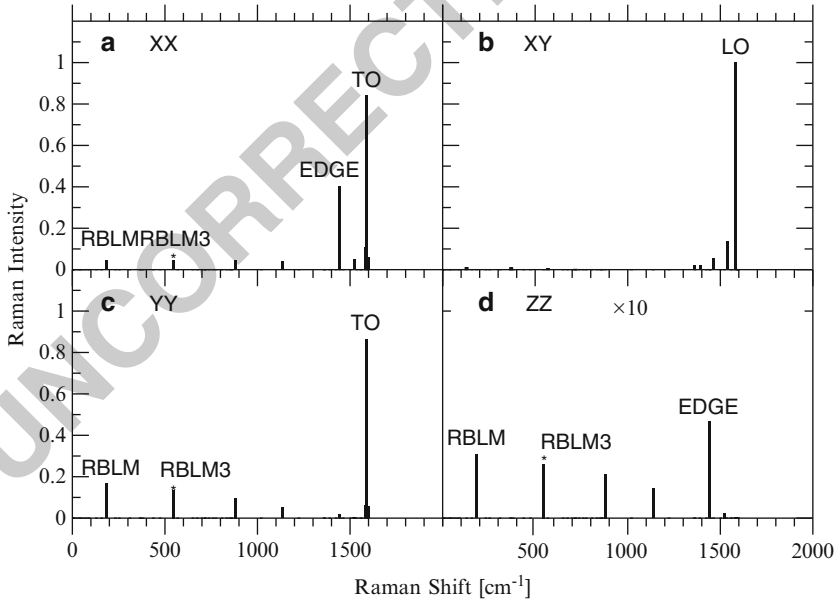

Fig. 2.14 The nonresonance Raman spectra of an $N = 9$ zigzag nanoribbon for the scattering geometries of (**a**) $zXX\bar{z}$, (**b**) $zXY\bar{z}$, (**c**) $zYY\bar{z}$, and (**d**) $yZZ\bar{y}$. The Raman intensity in each spectrum is normalized to the one for the largest Raman signal for the four indicated scattering geometries. The ZZ signals in (**d**) are 10 times enlarged relative to the other geometries [65]

UNCORRECTED PROOF

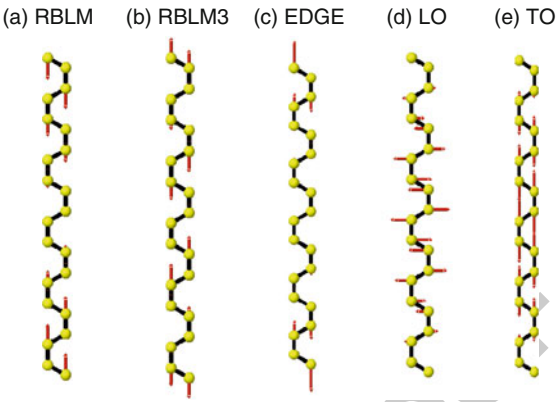

Fig. 2.15 Phonon eigenvectors of an $N = 11$ zigzag nanoribbon for (**a**) RBLM, (**b**) RBLM3, (**c**) Edge, (**d**) TO, and (**d**) LO phonon modes [65]

phenomena (the Kohn anomaly) and in this way we can assign LO and TO for graphene edges.

The vibrational direction of the edge states for a zigzag nanoribbon is perpendicular to the zigzag edge direction, while that for the armchair nanoribbon is parallel to the armchair edge. This difference of the vibrational direction can be enhanced by terminating the dangling bond by other heavy element such as F atoms. The edge phonon frequency of the zigzag edge is around 1,450 cm^{-1}, which is consistent with previous calculations [69] and experiments [57]. Two intermediate frequency spectra show higher RBLM modes with five and seven nodes.

2.3.4 *Polarization Dependence of the Raman Intensity*

To discuss the Raman intensity as a function of the polarization dependence and the edge dependence, we need to calculate the electron-optical transition amplitude. In Fig. 2.16, the square of calculated optical matrix elements $|M^{\mathrm{opt}}(\mathbf{A})|^2$ for the electromagnetic interaction of an electron in an optical field which depends on the vector potential $\mathbf{A}$ and the direction of the polarization of the laser light Θ is plotted as a function of the angle Θ relative to the edge of the nanoribbon [70].

Here, $\Theta = 0$ corresponds to the polarization of $\mathbf{A}$ (or electric field) being parallel to the edge. In this case, the amplitude $M^{\mathrm{opt}}(\mathbf{A})$ (or dipole vector in reference [64]) is given by [70]

$$M^{\mathrm{opt}}(\mathbf{A}) = \langle \Psi^{\mathrm{c}}_{\mathbf{k}} | H^{\mathrm{em}}_{\mathrm{K}} | \Psi^{\mathrm{v}}_{\mathbf{k}} \rangle, \tag{2.7}$$

where $\Psi^{\mathrm{v}}_{\mathbf{k}}(\mathbf{r})$ is the wave function in the valence energy band, which is related to that in the conduction energy band $\Psi^{\mathrm{c}}_{\mathbf{k}}(\mathbf{r})$ via $\Psi^{\mathrm{v}}_{\mathbf{k}}(\mathbf{r}) = \sigma_z \Psi^{\mathrm{c}}_{\mathbf{k}}(\mathbf{r})$ and $H^{\mathrm{em}}_{\mathrm{K}} = -v_{\mathrm{F}} e \sigma \cdot \mathbf{A}$ is the perturbation Hamiltonian of the optical dipole transition and v_{F} and σ are, respectively, the Fermi velocity of graphene and the Pauli matrix which operates on the wave functions at the edges [70]. Using the wave functions at zigzag and

UNCORRECTED PROOF

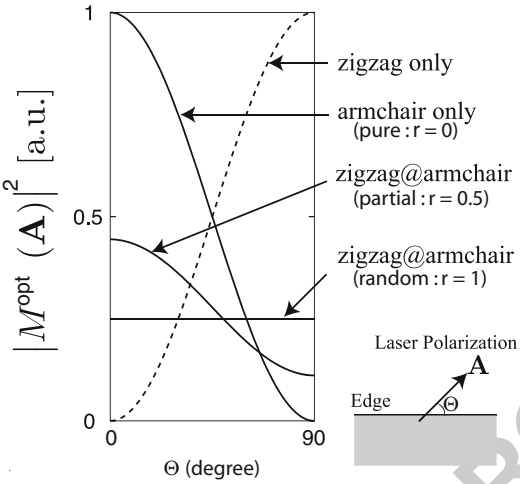

Fig. 2.16 The polarization dependence of the square of the optical transition amplitude ($|M^{\text{opt}}(\mathbf{A})|^2$) is plotted as a function of the angle of laser polarization (Θ) with respect to the orientation of the edge. For a pure zigzag (armchair) edge, as shown by the *dotted* (*solid*) line at the top) the intensity is a maximum when the laser polarization is perpendicular (parallel) to the edge. "zigzag@armchair" denotes the case when a small fraction of zigzag edges is introduced into part of a perfect armchair edge. Here the parameter of r means randomness with $r = 0$ (armchair only), $r = 0.5$ (partial), and $r = 1$ (random: a mixture of zigzag and armchair edges) [70]

armchair edges which consist of incident and reflecting waves at each edge, we can obtain the polarization (Θ) dependence of $M^{\text{opt}}(\mathbf{A})$.

In the case of pure zigzag edges (dotted line at the top of Fig. 2.16), the Raman intensity is proportional to $|M^{\text{opt}}(\mathbf{A})|^2 \propto \sin^2\Theta$, while for the pure armchair edges (solid line), $|M^{\text{opt}}(\mathbf{A})|^2 \propto \cos^2\Theta$. In the case of a general graphene ribbon, the edge consists of short segments of zigzag and armchair edges. Here we introduce a randomness factor r into the components of zigzag edges in the armchair edges (zigzag@armchair) in which $r = 0$ corresponds to the pure armchair edges and $r = 1$ is a completely random mixture of zigzag and armchair edges. In Fig. 2.16, we show $|M^{\text{opt}}(\mathbf{A})|^2$ vs. Θ for three different r values. It is clear that there is no angle Θ dependence for $r = 0$, since in this case the dependence would be the sum of $\cos^2\Theta + \sin^2\Theta$ which is unity. In an actual measurement of this polarization dependence, we can get results for intermediate polarization dependencies such as $r = 0.5$, which is consistent with the recent experiments [71, 72].

For distinguishing between LO and TO phonon modes, the phonon softening effects observed for LO mode in graphene (the Kohn anomaly) can be used. Depending on the intravalley and intervalley scattering at the armchair or zigzag edges, the occurrence of the Kohn anomaly shows clear edge differences. In Table 2.1, we show a list of the expected Raman signal (Raman), the occurrence of the Kohn anomaly (Kohn), and the polarization effect for zigzag edges, armchair edges, and the interior region of graphene. The detailed derivation of this calculation

UNCORRECTED PROOF

Table 2.1 Dependencies of the Raman intensities and Kohn anomalies on the Γ point optical phonon modes. The symbols ◯ and × for the Raman intensity and the Kohn anomaly represent "occurrence" and "absence," respectively. There is asymmetry between the Raman intensity and the Kohn anomaly; that is, the Kohn anomaly occurs only for the LO mode, while the mode with a strong Raman intensity changes according to the edge shape. The Raman intensity is enhanced when the polarization of the incident laser light is parallel (LO) to the armchair edge or when it is perpendicular (TO) to the zigzag edge [70]

Position	Mode	Raman	Kohn	Polarization
Zigzag	LO	×	◯	×
	TO	◯	×	◯
Armchair	LO	◯	◯	◯
	TO	×	×	×
Bulk	LO	◯	◯	◯
	TO	◯	◯	◯

is discussed in [70]. From Table 2.1, if we get a G-band signal without phonon softening, we can say that the Raman spectra comes from the TO phonon modes at zigzag edges, while the phonon softening (around 30 cm^{-1}) that occurs in the Raman spectra comes from the LO phonon modes at armchair edges, whose behavior is observed in a graphene with two edges that differ by an angle of 30° between them [58].

2.4 The Fermi Energy Dependence: The Kohn Anomaly

Next we discuss the effect of doping on the G band of single-layer graphene in Sect. 2.4.1, and the corresponding effect of doping on the G band of double-layer graphene is explicitly considered in Sect. 2.4.2.

2.4.1 Effect of Gate Doping on the G-Band of Single-Layer Graphene

In Fig. 2.17, the G-band spectra of single-layer graphene as a function of gate voltage is shown [73]. For achieving high doping levels, electrochemical doping is often used. The G-band frequency is upshifted ((a) and (b)) and the spectral width decreases (see (c)) by doping, as predicted by time-dependent perturbation theory in which the phonon frequency downshifts as a result of the electron–phonon interaction. This effect is known as the Kohn anomaly [29, 30, 58, 74, 75]. In the electron–phonon interaction, an electron–hole pair is virtually excited by a phonon near the Fermi energy. The gate voltage dependence of the Raman frequency in Fig. 2.17 comes from the fact that either the initial (or final) states for electron–hole pair excitation becomes empty (or occupied) for hole (electron) doping and that the corresponding perturbation processes are suppressed. The lower (higher) energy excitation of the electron–hole pair below (above) $\hbar\omega_G/2$, where ω_G is

UNCORRECTED PROOF

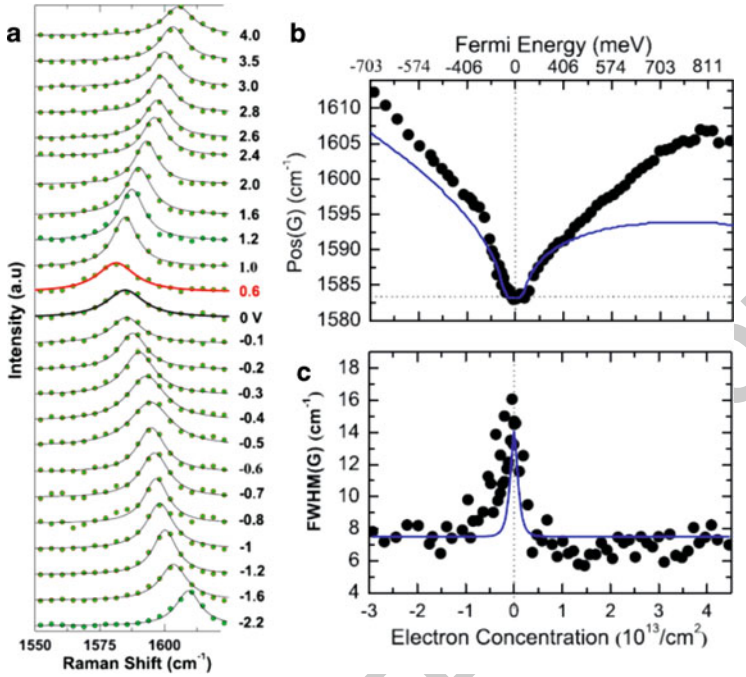

Fig. 2.17 The Raman G peak of doped monolayer graphene. (**a**) The G-band spectra observed at 295 K for many values of the gate voltage V_g. The darkened spectrum corresponds to the undoped case. (**b**) The G peak position (frequency) and (**c**) the linewidth as a function of electron concentration are deduced from the applied gate voltage data. *Black circles*: measurements; *solid line*: finite-temperature non-adiabatic calculation (Adapted from [73].)

the G-band phonon frequency, contributes to phonon hardening (softening). Thus the phonon softening becomes a maximum when the Fermi energy is located at $\hbar\omega_G/2$ from the Dirac point energy. The two anomalies at $\pm\hbar\omega_G/2$ are not clearly seen in this experiment due to temperature-induced broadening. However, a gate voltage dependence for the G-band frequency ω_G was measured at $T = 12\,\mathrm{K}$, where phonon anomalies at $E_g = \pm\hbar\omega_G/2$ could be clearly distinguished [76]. The 12 K experiment was, however, carried out on bilayer graphene, where another interesting effect occurs, as described in Sect. 2.4.2. The broadening of the Raman spectra comes from the shortening of the lifetime of the G-band phonon by the electron–phonon interaction, and thus the broadening should be a maximum around the Dirac point energy, as is confirmed experimentally in Fig. 2.17c.

Using the pseudospin and the field for the pseudospin [51, 52], Sasaki et al. gave an analytic formula for the electron–phonon interaction for the LO and TO phonon modes for carbon nanotubes [33] and graphene [58]. Although we do not here go into detail regarding this theory, this theoretical analysis will be useful for gaining a general understanding of both the Raman spectra and the physical properties of graphene.

UNCORRECTED PROOF

2.4.2 *Effect of Gate Doping on the G Band of Double-Layer Graphene*

The gate doping of double-layer graphene in particular has been investigated by many groups. Part of the interest focuses on the fact that double-layer graphene may exhibit an energy gap under the application of an electric field perpendicular to the graphene surface, which can be used to vary the Fermi level. This effect is important for the application of double-layer graphene for semiconductor devices. Thus the characterization of the Raman spectra of gated double-layer graphene has become an important research topic.

In bilayer or double-layer graphene, the unit cell has four C atoms which gives two π and two π^* energy bands at the K point (see Fig. 2.18). In this case, there will be more than two Kohn anomalies in the G band depending on how the two π bands are occupied by doping (see the right-hand side of Fig. 2.18) [73, 76]. When the Fermi energy reaches $\pm\hbar\omega_G/2$, the $\pi-\pi^*$ transition shown in Fig. 2.18(I) is no longer allowed, as it is in single-layer graphene, but the transition from the now filled lowest energy π^* band to the higher energy π^* band, shown in Fig. 2.18(II), is possible. When the gate voltage rises further and reaches the second π^* band, another singular behavior now occurs in the renormalization process, as shown in Fig. 2.18(III). These effects are seen in the G-band frequency and linewidth of bilayer graphene (see Fig. 2.18), where a distinctly different behavior with respect to the monolayer case (see Fig. 2.17) is clearly observed for both the frequency and linewidth. Therefore, when discussing graphene systems above, we see that the renormalization effect changes significantly in going from single to bilayer graphene, and it would change further by increasing the number of layers, although the renormalization effect will become less and less evident with increasing layer number.

In the case of double-layer graphene, the G-band phonon is split into symmetric (S) and antisymmetric (AS) components corresponding to the symmetry between the upper and lower graphene layers, as shown in Fig. 2.19b [77]. An important point is that the electron-hole excitations for the S and AS G-band phonons are different for the two π^* energy bands [77, 78] (see Fig. 2.20). For electron and hole pair creation by a phonon that couples the π_1 and π_1^* energy bands, only the S symmetry component of the G band is coupled by the electron–phonon interaction (Fig. 2.20a), while for hole doping (Fig. 2.20b) both the S and AS G-band phonons are coupled. Thus an asymmetric behavior in the phonon softening effect appears for electron and hole doping, as shown in Fig. 2.19a.

2.5 Near-Field Raman Spectroscopy

The last subject of Chap. 2 is near-field Raman spectroscopy. The investigation of sp^2 carbons via conventional Raman spectroscopy has usually been limited by the spatial resolution of usual confocal systems. The spatial resolution Δx of a standard

UNCORRECTED PROOF

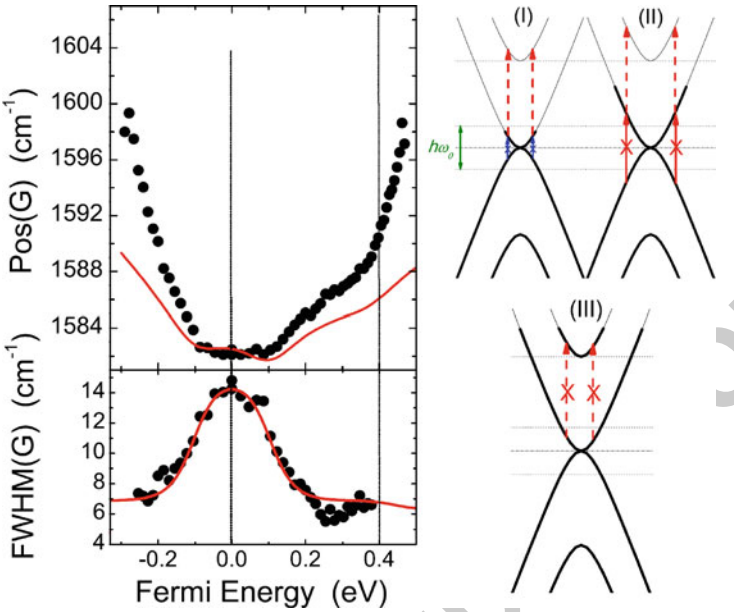

Fig. 2.18 Position of the peak frequency [Pos(G)] and the linewidth [FWHM(G)] measured at full width half maximum intensity for the Raman *G*-band feature of doped bilayer graphene. *Black circles*: measurements; *thin line*: finite-temperature nonadiabatic calculation. On the *right*, schematics of the electron–phonon coupling at three different doping levels, as indicated by the *thicker lines* on the electronic bands (Adapted from [73].)

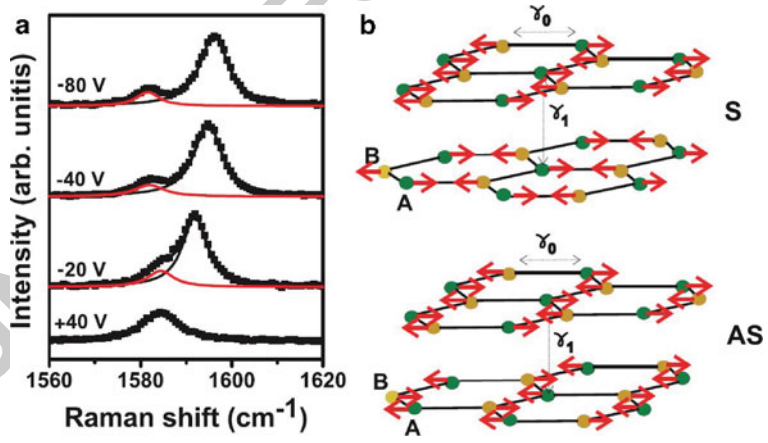

Fig. 2.19 (**a**) Raman *G* band of bilayer graphene for –80 V, –40 V, –20 V and +40 V gate voltages. Two Lorentzian curves (corresponding to the different displacements of the carbon atoms in (**b**)) are needed to fit the *G* band for –80 V, –40 V, and –20 V. (**b**) Displacement of the atoms for the S and AS symmetry phonon modes in bilayer graphene [77]

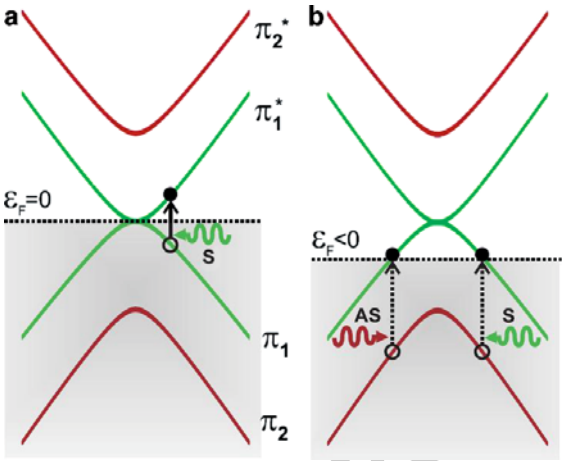

Fig. 2.20 Parabolic band structure of bilayer graphene near the K point where the Fermi level is indicated by the *dotted horizontal line*. The *vertical arrows* illustrate the possible transitions induced by symmetric (*green*) and antisymmetric (*red*) $q \neq 0$ phonons for (**a**) interband electron–hole pair creation and (**b**) intraband electron–hole pair creation. The gap opening in bilayer graphene is not considered in this diagram [77]

optical microscope is limited by diffraction to roughly the Abbé criterion [79]:

$$\Delta x = \frac{0.61\lambda}{\mathrm{NA}}, \tag{2.8}$$

where λ is the wavelength of light and NA is the numerical aperture of the objective lens. Although the NA can be optimized by performing experiments in a medium with a large index of refraction n that surrounds the sample, or by engineering objectives with large collection angles, conventional microscopes can only achieve resolutions on the order of $\lambda/2$ ($\geq$200 nm). As a consequence, the investigation of structural details at the mesoscopic level becomes a difficult task for Raman spectroscopists.

Tip-enhanced near-field Raman spectroscopy (TERS) [80] has, however, provided an alternative way to overcome this barrier by performing spectroscopic imaging with ultrahigh spatial resolution. TERS studies on sp^2 carbons have been limited mostly to carbon nanotubes until now [79,81–89], while strong enhancement effects in two-dimensional systems are unlikely. However, the use of TERS to study disorder in carbon nanotubes, as discussed in this text, has been largely successful. For this reason, we here discuss the basics for the TERS approach in one-dimensional systems, and some interesting results on carbon nanotubes are presented.

2.5.1 The Spatial Resolution in Optical Microscopes

In general, conventional optical systems are not able to collect the whole spectrum of spatial frequencies associated with optical fields generated by a light source located at a distance sufficiently far from the detector (far-field regime). The angular

UNCORRECTED PR

spectrum representation of a scattered electric field E_s in a plane $z = \text{const.}$ far from the light source is given by [79]

$$E_s(x, y, z) = \int \int_{-\infty}^{\infty} \hat{E}_s(k_x, k_y; 0) e^{i(k_x x + k_y y)} e^{\mp i k_z z} dk_x dk_y, \tag{2.9}$$

where k_x, k_y, and k_z are the spatial frequencies related to the Cartesian coordinates x, y, and z, respectively, and $\hat{E}_s(k_x, k_y; 0)$ are the Fourier amplitudes of the electric field at $z = 0$.

The exponential term $e^{\mp i k_z z}$ in (2.9) influences the propagation of the electric field E_s along the z-axis. The k-vector (k_x, k_y, k_z) and the frequency $\omega = 2\pi c/\lambda$ are related by the free-space dispersion relation, and hence k_z is given by [79]

$$k_z = \sqrt{(2\pi n/\lambda)^2 - k_\parallel^2}, \tag{2.10}$$

where we have defined $k_\parallel^2 = k_x^2 + k_y^2$. According to (2.9) and (2.10), for $k_\parallel \leq 2\pi n/\lambda$, the wave vector k_z is a real number. In this case, the electric field E_s propagates along the z-axis oscillating with $e^{\mp i k_z z}$, giving rise to the far-field component of the optical field. On the other hand, if $k_\parallel > 2\pi n/\lambda$, the wave vector k_z becomes an imaginary number, and the electric field E_s decays exponentially along the z direction. If the image plane at $z = \text{const.}$ is sufficiently well separated from the source at $z = 0$, the contribution from this decaying part (evanescent waves) will be lost. Therefore, there is always a loss of information between the near-field and the far-field optical limits.

2.5.2 *The Principle of TERS*

The goal of tip-enhanced Raman spectroscopy (TERS) is to obtain the spectral response from nanoscopic structures with an optical resolution beyond the diffraction limit. For this purpose, a sharp metal tip is placed sufficiently near the sample surface [90,91]. The tip provides a channel through which the near-field components of the scattered light (evanescent waves) become propagating waves in the far zone. In other words, by using a confined source field with a large bandwidth of spatial frequencies, the high spatial frequencies generated by the sample become accessible in the far field, and the spatial resolution is defined by the diameter of the tip apex [80]. However, there is a fundamental issue involved in such an experiment, which is the fact that the signal generated by the near-field and far-field components of the scattered light will be intermixed in the far zone. To solve this issue, the tip might be able to perform its secondary function, which is to enhance the optical fields generated in the near-field regime.

UNCORRECTED PROOF

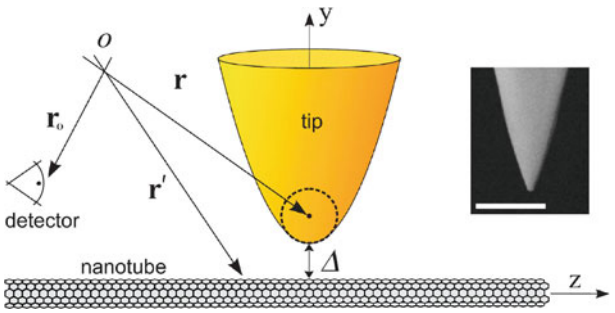

Fig. 2.21 Schematics for the spatially resolved Raman scattering by a carbon nanotube. The position vectors $\mathbf{r}$, $\mathbf{r}'$, and $\mathbf{r}_o$ denote the location of the center of the tip apex, the Raman dipole moment $\mathbf{p}$, and the detector, respectively. The *dashed circumference* represents a small sphere of radius r_{tip} centered at the tip apex, and ´ is the distance between the tip and the nanotube. The *inset* depicts an SEM image of the gold tip used in the experiment, where the scale bar denotes 200 nm [92]

2.5.3 Mechanism of Near-Field Enhancement

This section provides a brief analytical theory for local field enhancement. The theory is given in terms of one-dimensional (1D) systems, which can be directly applied to the well-studied carbon nanotubes [92].

Figure 2.21 shows the experimental configuration and the coordinates used in the theoretical analysis. The electric field $\mathbf{E}$ near the laser-irradiated gold tip is axially symmetric and interacts locally with a single wall carbon nanotube (SWNT) at frequency ω. The induced dipole $\mathbf{p}$ per unit length at the Raman frequency ω_s and at location $\mathbf{r}'$ can be represented as [92]

$$\mathbf{p}(\mathbf{r}', \omega_s) = \boldsymbol{\alpha}^R(\mathbf{r}'; \omega_s, \omega)\, \mathbf{E}_{tot}(\mathbf{r}' - \mathbf{r}; \omega), \tag{2.11}$$

where $\mathbf{r}$ denotes the position of the center of the tip apex, $\boldsymbol{\alpha}^R$ is the Raman polarizability (per unit length), and $\mathbf{E}_{tot}$ is the total electric field interacting with the electron density at $\mathbf{r}'$ in the carbon nanotube.

The analysis that we discuss here applies to one-phonon Raman processes involving vibrations belonging to the totally symmetric A_{1g} irreducible representation which could describe the radial breathing mode and the lower and upper components G^- and G^+ of the G band. In this case, the Raman polarizability tensor $\boldsymbol{\alpha}^R$ is written as [92]

$$\boldsymbol{\alpha}_q^R = \begin{bmatrix} \alpha_{\perp,q}^R & 0 & 0 \\ 0 & \alpha_{\perp,q}^R & 0 \\ 0 & 0 & \alpha_{\parallel,q}^R \end{bmatrix}, \quad q \in \{\mathrm{RBM}, \mathrm{G}^+, \mathrm{G}^-\}. \tag{2.12}$$

UNCORRECTED PROOF

The field $\mathbf{E}_{\text{tot}}$ in (2.11) is the sum of the external driving field $\mathbf{E}$ and screening fields due to neighboring charges, where the depolarization effect has to be considered. The external driving field $\mathbf{E}$ corresponds to the superposition of the incident laser field $\mathbf{E}_{\text{o}}$ and the localized field generated by the gold tip acting as an optical antenna. Close to the tip apex, the external driving field $\mathbf{E}(\mathbf{r}';\omega)$ resembles the field of an induced dipole $\boldsymbol{\mu}$ located at the center of a small sphere of radius r_{tip} (location $\mathbf{r}$ in Fig. 2.21).

Analysis of the above fields lead to an expression for determining the near-field enhancement as a function of the tip–sample distance Δ. Considering that near-field (NF) and far-field (FF) components are always intermixed, the relative intensity of the scattered signal is given by the sum of these two contributions, i.e., $I/I_{\text{max}} = (I_{\text{FF}} + I_{\text{NF}})/I_{\text{max}}$. Crossterms originating from the interference between the FF and NF components can be neglected. The ratio $I_{\text{max}}/I_{\text{FF}}$ corresponds to the maximum Raman enhancement factor M, which allows us to represent the relative intensity of the scattered signal as [92]

$$\frac{I}{I_{\text{max}}} = \frac{1}{M} + \frac{C}{(´ + r_{\text{tip}})^{10}}. \tag{2.13}$$

The M, C, and r_{tip} parameters are to be determined by fitting experimental data, while r_{tip} has to be related to the tip geometry. What is remarkable here is that theory predicts that near-field Raman intensity is inversely proportional to the 10th power of the tip–sample distance, thereby providing a large enhancement of spatial details.

2.5.4 Application to Carbon Nanotubes

Advances in the science of carbon nanotubes generated by tip-enhanced Raman measurements include the detection of local defects, chirality changes, and local dopants [86–89]. The technique of tip-enhanced Raman spectroscopy can be readily applied to study nanostructured features appearing in monolayer or bilayer graphene or at the edges of graphene nanoribbons.

Figure 2.22a shows a large-scale confocal Raman image of a self-organized carbon nanotube serpentine [92]. The contrast (color scale) in the image renders the intensity of the graphitic (C–C stretching) G band ($\sim$1,580 cm^{-1}). Figure 2.22b shows a confocal Raman image corresponding to the G-band intensity acquired in the boxed area in Fig. 2.22a. Figure 2.22c shows the near-field image recorded in the same area as panel (b). The resulting resolution of 25 nm is defined by the tip radius. A linecut along the dashed line in image Fig. 2.22c is depicted in Fig. 2.22d. It is evident that near-field imaging not only improves the resolution but also improves the signal-to-noise ratio.

Figure 2.22e shows the corresponding Raman spectra for the smallest ($\sim$2 nm) and largest ($\sim$38 nm) tip–sample separation. The two spectra are offset for clarity. The radial breathing mode (RBM) frequency $\omega_{\text{RBM}} = 262\,\text{cm}^{-1}$ identifies the sample as a semiconducting tube whose energy gap for the second $E_\mu \rightarrow E_\mu$

UNCORRECTED PROOF

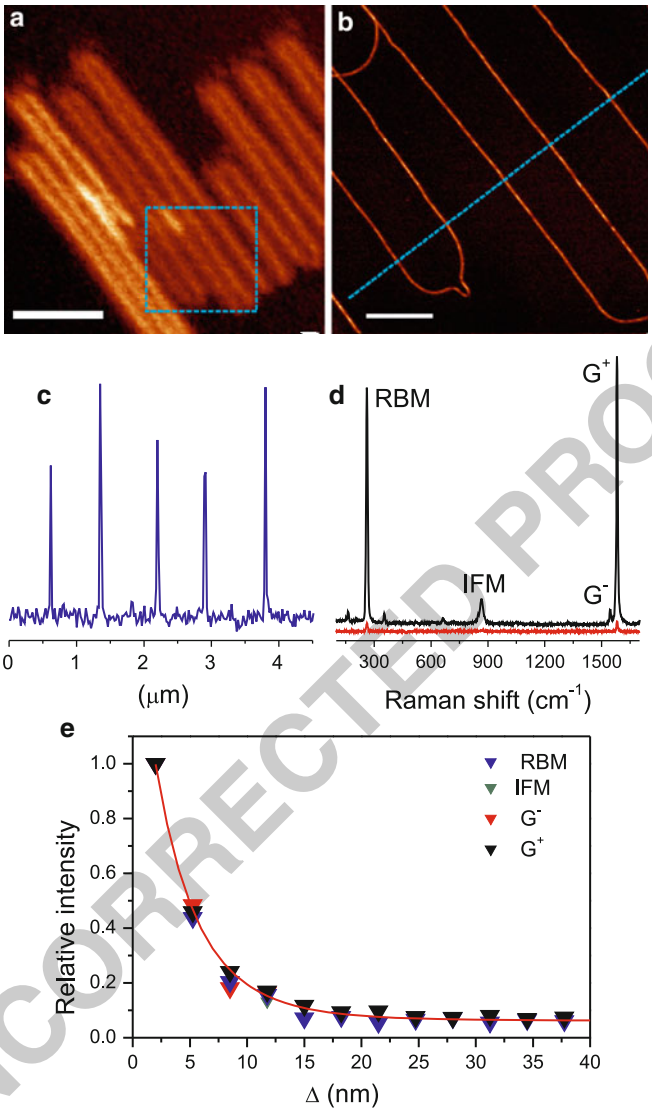

UNCORRECTED PROOF

Fig. 2.22 (**a**) Confocal Raman image corresponding to the *G*-band intensity of a semiconducting nanotube. The scale bar denotes 6 μm. (**b**) Confocal Raman image corresponding to the *G*-band intensity recorded in the boxed area in panel (**a**). (**c**) Near-field Raman image corresponding to the *G*-band intensity recorded in the same area as panel (**b**). The scale bars in panels (**b**) and (**c**) denote 800 nm. (**d**) Intensity profile obtained along the *dashed line* in panel (**c**). (**e**) Far-field Raman spectrum (*red curve*) and near-field Raman spectrum (*black curve*) recorded at the largest (∼38 nm) and smallest (∼2 nm) tip–sample separation, respectively. (**f**) Approach curves for the intensity of the RBM, IFM, G^- and G^+ phonon bands vs. Δ in Fig. 2.22 [92]

optical transition is in resonance with the incident laser energy. The near-field spectrum also clearly features the intermediate frequency mode (IFM) occurring at 865 cm^{-1}, and the G^- and G^+ peaks occurring at 1,545 cm^{-1} and 1,585 cm^{-1}, respectively. Notice that the disorder-induced D band ($\sim$1,350 cm^{-1}) is so weak that it cannot be observed, indicating that the serpentine nanotube has a very low defect density. Within the experimental resolution, no differences in the lineshape and resonant frequency of any phonon bands are observed for the far-field and near-field Raman spectra.

Figure 2.22f shows the intensities (integrated areas) of several Raman peaks as a function of the tip–sample separation Δ. All Raman intensities are normalized to the corresponding values at shortest separation ($\Delta \sim 2$ nm). The red curve in Fig. 2.22f is a fit to the experimental data according to (2.13). It can be seen from Fig. 2.22f that the theoretical predictions from [92] are in good agreement with the experimental data. The fitting parameters obtained were $M = 16$, $C = 4.5\times10^{15}\,\mathrm{nm}^{10}$, and $r_{\mathrm{tip}} = 35$ nm. All the Raman modes show the same distance dependence, that is, within the resolution of these measurements, all phonon modes get enhanced by the same factor.

2.6 Summary and Perspective

In summary, recent studies on graphene and sp^2 carbons and defects in these systems have significantly advanced our understanding of how Raman spectroscopy can be used to characterize these material systems. Powerful new experimental techniques such as near-field Raman spectroscopy have become available and have been applied to these materials, and at the same time new theoretical works using the pseudospins of graphene have pushed graphene research in new directions. Especially important also has been the advances in the fabrication and processing of graphene ribbons and their subsequent annealing to form well-defined and stable armchair and zigzag edge structures. Because of the well-defined edge structures that can now be prepared, the theoretical investigation of electron–phonon and electron–photon interactions at the edges can be formulated much better analytically, and theoretical results can now be compared directly with experiments.

Near-field measurements of the Raman spectra of carbon nanotubes have greatly enhanced the spatial resolution which can now be achieved, reaching resolutions much smaller than the wavelength of light. This means that a scanning Raman image can now be directly compared with observations made with other high spatial resolution techniques, such as transmission electron microscopy, scanning probe microscopy (SPM), and x-ray Photo emission spectroscopy (XPS) imaging. Since we now know much more about the physics of the electron–phonon interaction, we can now tune the electron–phonon interaction by varying the Fermi energy. This can be accomplished reliably using electrochemical doping, which now becomes a new parameter that can be varied controllably during Raman spectroscopy experiments. Varying the gate voltage using back gates or top gates or both at once in taking the

UNCORRECTED PROOF

Raman spectra is now allowing researchers to obtain a better understanding of the Raman spectral width and phonon softening phenomena associated with the Kohn anomaly in both graphene and metallic carbon nanotubes. These techniques are also important for characterizing the Fermi energy position in graphene devices. In the future, we can imagine a possible application of using a Raman signal as a sensor for monitoring the behavior of devices as a function of the gate voltage.

An essential factor in the Raman spectroscopy of carbon nanotubes is the resonance condition for the optical transition energies which can be used to specify the geometrical structure of a SWNT through their one-dimensional van Hove singularities. The Raman intensity of SWNTs is determined by how close the optical transition energies are to the laser light energy $\hbar\omega$, while the resonance width in the Raman excitation profile provides an important parameter for observing the Raman signal of a SWNT for a given laser excitation energy even though the Raman intensity (through the exciton–photon and exciton–phonon interactions) is strongly chirality dependent. On the other hand, in the case of graphene, there are no one-dimensional van Hove singularities for optical transitions except for the case of a very narrow graphene ribbon which would be denoted as a graphene nanoribbon. Such graphene nanoribbons can be considered as a one-dimensional system with properties somewhat analogous to a carbon nanotube except that the graphene nanoribbon has edges which have interesting properties as described elsewhere [26]. The effective resonance condition of an infinite graphene sheet is satisfied for any value of the laser excitation energy. Thus, although the Raman signal of single layer graphene is not as strong as that for SWNTs, we can always get a Raman signal for any number of layers of graphene and for any laser energy that promotes an electron from an occupied state to an empty state. In this sense, the relative Raman intensity depends not on the resonance condition but primarily on the Raman tensor and the electron–phonon interaction. Since the electron–phonon interaction is known to be anisotropic in k space, especially around the K point in the two dimensional Brillouin zone, the analysis of this anisotropy of the electron–phonon interaction can be used to determine the edge direction relative to the polarization of the light, and in particular to distinguish between armchair and zigzag edges. Enhancement of the Raman intensity for graphene is needed for carrying out quick measurements of the Raman spectra, and in such cases tip-enhanced and/or interference-enhanced Raman spectra can now be used to enhance the spatial resolution of pertinent Raman features.

An important issue for discussing the difference between SWNTs and graphene is the dimensionality of the materials because the effect of the Coulomb interaction plays a different role in 2D graphene relative to 1D SWNTs. For example, in SWNTs, the exciton is essential for describing the photoexcited electron and hole pair, whereas an electron and hole are freely moving in graphene and therefore localization effects are less important. Nevertheless, it is expected that the Coulomb interaction in graphene will be studied in detail in the near future through investigation of the photo-current and electronic transport near the Fermi energy, and the origin of the asymmetric lineshapes observed in the Raman spectra (known as Breit–Wigner–Fano lineshapes) should then be further elucidated in the near future.

UNCORRECTED PROOF

Ion bombardment measurements have provided us with important information about the area of the Raman-active spatial regions that are associated with the D-band Raman signal. This spatial region is closely related to the phase coherence length (or area) for an electron in which the electron retains its information about the phase of the wave function throughout the elastic scattering events experienced by the electron in the D-band scattering processes. In fact, an interference effect between the incident and scattered electrons at a graphene edge gives selective Raman signals for LO and TO phonon modes, which allows one to distinguish between armchair and zigzag edges by applying theoretical considerations to the interpretation of such Raman spectra. Microscopic analysis of the elastic scattering will become more important in the future in the study of the D-band spectra for different nanostructures containing defects originating from different types of defects (interstitial atoms, impurity atoms, line defects vs. point defects, etc.). The systematic generation of specific types of defects should provide a key approach for obtaining defect type-related information in the Raman spectra through, for example, joint Raman and TEM studies. We can therefore expect that in the future we will be doing more systematic studies on point defects in graphene as a function of ion species of different atomic species, different isotopes of ions with the same atomic number, ions with different energies, etc. The present studies, as described above, of defects in graphene associated with point defects caused by ion implantation already constitute a broad subject. But this is only the beginning. There are many different kinds of defects that can be produced in graphene and carbon nanotubes such as vacancies, divacancies, interstitial atoms of the same or different species, and complexes of impurity/vacancy pairs. Systematic studies of such effects by Raman spectroscopy can teach us a lot about graphene and carbon nanotubes as well as the potential of what Raman spectroscopy can teach about each of these types of defects as they occur in a simple well-characterized system like graphene.

Also in the realm of future work are major opportunities to use the controlled and systematic introduction of defects, such as by ion implantation, into bilayer graphene, for Raman characterization studies, as has been discussed above for monolayer graphene. For bilayer graphene, for example, it would be interesting also to study Raman spectra comparatively from the sample face exposed to the ion beam and from the back side of the sample. The major differences in the electronic structure of monolayer graphene, with its linear $E(k)$ relation, and of bilayer graphene, with its quadratic dispersion relation, could show different behaviors of interest with regard to the modifications of these electronic structures through the introduction of defects.

Another area for future work would be a systematic Raman study of the controlled defects introduced into graphene nanoribbons by ion implantation where the defects could be confined, for example by the use of masks, to the interior of the ribbons or to the edges, including such studies on both zigzag and armchair edges. Graphene nanoribbons are important as a means for introducing band gaps into graphene, with electronic and transport properties that depend on the width of the ribbon as well as on the crystalline orientation and the quality of the structure

UNCORRECTED PROOF

established at each of the edges.[26] Combined transport, Raman, and electron microscopy measurements would likely prove highly informative for such studies. Thus many research opportunities remain open for exploration in the systematic study of defects, edges, and the defect/edge combination in monolayer and bilayer graphenes. The exploration of the special properties of trilayer graphene is presently a largely unexplored arena.

Raman spectroscopy has been used successfully for characterizing carbon materials for many years both in research laboratories and industrially. Thus we expect that Raman spectroscopy and graphene will become increasingly important as more industrial applications of graphene and sp^2 carbons are found. As more industrial applications are found, the demands for developing standards for describing the quality of graphene materials will increase. Making a thin graphene ribbon with a small width introduces an energy gap. Therefore we can expect graphene ribbons to become more important for applications just because the use of ribbons with narrow widths introduce an energy gap. Furthermore controlling the edge structure of the graphene ribbon so that the edge is atomically smooth allows the introduction of well-defined armchair and zigzag edges [26] with well-defined electronic properties. Thus we can expect increasing attention to be given to Joule heating techniques for increasing the structural perfection of edges and we can expect more use to be made of enhanced edge passivation by functionalization. We can also expect to see more use of multiple measurement techniques including Raman spectroscopy for the characterization of graphene and sp^2 carbon materials based on promising work that has already been carried out using multiple characterization techniques. Many applications would like to combine the exceptional properties of graphene with the special properties of a semiconducting material with a band gap, and for this reason we can expect thin narrow graphene ribbons to receive increasing attention.

Even within the scope of what is discussed in this chapter, many topics relevant to defects in graphene and carbon nanotubes that have already been studied and documented in the literature have not been discussed here. For example, we did not describe time-dependent phenomena relevant to Raman spectroscopy in graphene, or in other carbon nanostructures, nor did we discuss coherent phonon measurements in which the transmission of the probe light is vibrating at frequencies where phonons are excited coherently. This is a large research field with many interesting regimes depending on the pulse length and intensity. Combining the polarization dependence measurements with coherent phonon measurements should yield important information about the defect type and its special characteristics, but such studies remain as work for the future. Further, we did not mention measurements that have been made on the stress and temperature dependence or the electrochemical dependence of the Raman signal which are also very promising probes that can be used for characterizing the local physical properties of graphene and carbon nanotubes.

Acknowledgements AJ and LC acknowledge MCT-CNPq and the AFOSR/SOARD Project (Award No. FA9550-08-1-0236). MSD acknowledges NSF Grant No. DMR-07-04197. R.S. Acknowledges MEXT Grant No. 20241023.

UNCORRECTED PROOF

References

1. L.M. Malard, M.A. Pimenta, G. Dresselhaus, M.S. Dresselhaus, Phys. Rep. **473**, 51–87 (2009)
2. R. Saito, K. Sato, Y. Oyama, J. Jiang, Ge.G. Samsonidze, G. Dresselhaus, M.S. Dresselhaus, Phys. Rev. B **71**, 153413 (2005)
3. F. Tuinstra, J.L. Koenig, J. Phys. Chem. **53**, 1126 (1970)
4. F. Tuinstra, J.L. Koenig, J. Compos. Mater. **4**, 492 (1970)
5. R.J. Nemanich, S.A. Solin, Solid State Comm. **23**, 417 (1977)
6. R.J. Nemanich, S.A. Solin, Phys. Rev. B **20**, 392–401 (1979)
7. C. Kittel, in *Introduction to Solid State Physics*, 6th edn. (Wiley, New York, 1986)
8. N.W. Ashcroft, N.D. Merman, in *Solid State Physics*, (Holt Rinehart and Winston, New York, 1976), p. 141
9. A. Jorio, R. Saito, M.S. Dresselhaus, G. Dresselhaus, *Raman Spectroscopy in Graphene Related Systems* (Wiley, WeinHeim, 2010), vol. in press
10. M.A. Pimenta, G. Dresselhaus, M.S. Dresselhaus, L.G. Cançado, A. Jorio, R. Saito, Phys. Chem. Chem. Phys. **9**, 1276–1291 (2007)
11. A. Jorio, M.S. Dresselhaus, G. Dresselhaus, *Carbon Nanotubes: Advanced Topics in the Synthesis, Structure, Properties and Applications. Springer Series on Topics in Applied Physics* (Springer, Berlin, 2008), vol. 111
12. M.S. Dresselhaus, G. Dresselhaus, R. Saito, A. Jorio, Phys. Rep. **409**, 47–99 (2005).
13. M.S. Dresselhaus, R. Kalish, *Ion Implantation in Diamond, Graphite and Related Materials. Springer Series in Materials Science* (Springer, Berlin, 1992), vol. 22
14. T.P. Mernagh, R.P. Cooney, R.A. Johnson, Carbon **22**, 39–42 (1984)
15. M.M. Lucchese, F. Stavale, E.H. Ferriera, C.Vilane, M.V.O. Moutinho, R.B. Capaz, C.A. Achete, A. Jorio, Carbon **48**, 1592–1597 (2010)
16. R. Tsu, J. H. Gonzalez, I.C. Hernandez, Solid State Comm. **27**, 507 (1978)
17. R. Saito, A. Jorio, A.G. Souza Filho, G. Dresselhaus, M.S. Dresselhaus, M.A. Pimenta, Phys. Rev. Lett. **88**, 027401 (2002)
18. R.P. Vidano, D.B. Fishbach, L.J. Willis, T.M. Loehr, Solid State Comm. **39**, 341 (1981)
19. P. Lespade, A. Marchand, M. Couzi, F. Cruege, Carbon **22**, 375 (1984)
20. P. Lespade, R. Al-Jishi, M.S. Dresselhaus, Carbon **20**, 427–431 (1982)
21. H. Wilhelm, M. Lelausian, E. McRae, B. Humbert, J. Appl. Phys. **84**, 6552–6558 (1998)
22. C. Thomsen, S. Reich, Phys. Rev. Lett. **85**, 5214 (2000)
23. R. Saito, A. Grüneis, Ge.G. Samsonidze, V.W. Brar, G. Dresselhaus, M.S. Dresselhaus, A. Jorio, L.G. Cançado, C. Fantini, M.A. Pimenta, A.G. Souza Filho, New J. Phys. **5**, 157.1–157.15 (2003)
24. X. Jia, M. Hofmann, V. Meunier, B.G. Sumpter, J. Campos-Delgado, J.M. Romo-Herrera, H. Son, Y.-P. Hsieh, A. Reina, J. Kong, M. Terrones, M.S. Dresselhaus, Science **323**, 1701–1705 (2009)
25. T. Enoki, Y. Kobayashi, K.-I. Fukui, Int. Rev. Phys. Chem. **26**, 609–645 (2007)
26. X. Jia, J. Campos-Delgado, M. Terrones, V. Meunier, M.S. Dresselhaus, Nanoscale (2010)
27. A. Grüneis, R. Saito, T. Kimura, L.G. Cançado, M.A. Pimenta, A. Jorio, A.G. Souza Filho, G. Dresselhaus, M.S. Dresselhaus, Phys. Rev. B **65**, 155405-1–155405-7 (2002)
28. J. Jiang, R. Saito, A. Grüneis, S.G. Chou, Ge.G. Samsonidze, A. Jorio, G. Dresselhaus, M.S. Dresselhaus, Phys. Rev. B **71**, 045417-1–045417-19 (2005)
29. S. Piscanec, M. Lazzeri, M. Mauri, A.C. Ferrari, J. Robertson, Phys. Rev. Lett. **93**, 185503 (2004)
30. M. Lazzeri, F. Mauri, Phys. Rev. Lett. **97**(26), 266407 (2006)
31. K. Ishikawa, T. Ando, J. Phys. Soc. Jpn. **75**, 84713 (2006)
32. V.N. Popov, P. Lambin, Phys. Rev. B **73**, 085407 (2006)
33. K. Sasaki, R. Saito, G. Dresselhaus, M.S. Dresselhaus, H. Farhat, J. Kong, Phys. Rev. B **77**, 245441 (2008)

AQ4

UNCORRECTED PROOF

34. E.H. Martins Ferreira, M.V.O. Moutinho, F. Stavale, M.M. Lucchese, R.B. Capaz, C.A. Achete, A. Jorio, Phys. Rev. B (2010), Submitted for publication
35. A. Jorio, M.M. Lucchese, F. Stavale, E.H.M. Ferreira, M.V.O. Moutinho, R.B. Capaz, C.A. Achete, J. Phys. Condens. Matter **22**, 334204 (2010)
36. M. Lazzeri, C. Attaccalite, L. Wirtz, F. Mauri, Phys. Rev. B **78**, 081406R (2008)
37. K. Sato, R. Saito, Y. Oyama, J. Jiang, L.G. Cançado, M.A. Pimenta, A. Jorio, Ge.G. Samsonidze, G. Dresselhaus, M.S. Dresselhaus, Chem. Phys. Lett. **427**, 117–121 (2006)
38. L.G. Cançado, M.A. Pimenta, R.A. Neves, G. Medeiros-Ribeiro, T. Enoki, Y. Kobayashi, K. Takai, K. Fukui, M.S. Dresselhaus, R. Saito, A. Jorio, Phys. Rev. Lett. **93**, 047403 (2004)
39. L.G. Cançado, M.A. Pimenta, B.R. Neves, M.S. Dantas, A. Jorio, Phys. Rev. Lett. **93**, 247401 (2004)
40. L.G. Cançado, R. Beams, L. Novotny, Preprint at ⟨http://arxiv.org/abs/0802.3709⟩ (2008)
41. L.G. Cançado, K. Takai, T. Enoki, M. Endo, Y.A. Kim, H. Mizusaki, N.L. Speziali, A. Jorio, M.A. Pimenta, Carbon **46**, 272–275 (2008)
42. E.B. Barros, N.S. Demir, A.G. Souza Filho, J. Mendes Filho, A. Jorio, G. Dresselhaus, M.S. Dresselhaus, Phys. Rev. B **71**, 165422 (2005)
43. M. Fujita, K. Wakabayashi, K. Nakadw, K. Kusakabe, J. Phys. Soc. Jpn. **65**, 1920–1923 (1996)
44. K. Nakada, M. Fujita, G. Dresselhaus, M.S. Dresselhaus, Phys. Rev. B **54**, 17954–17961 (1996)
45. D.V. Kosynkin, A.L. Higginbotham, A. Sinitskii, J.R. Lomeda, A. Dimiev, B.K. Price, J.M. Tour, Nature **458**(7240), 872–876 (2009)
46. L. Jiao, L. Zhang, X. Wang, G. Diankov, H. Dai, Nature **458**, 877–880 (2009)
47. M.Y. Han, B. Özyilmaz, Y. Zhang, P. Kim, Phys. Rev. Lett. **98**, 206805 (2007)
48. T. Enoki K. Takai, Phys. Rev. Lett. **149**, 1144–1150 (2009)
49. K. Kusakabe M. Maruyama, Phys. Rev. B **67**(9), 92406 (2003)
50. L.M. Woods, G.D. Mahan, Phys. Rev. B **61**, 10651 (2000)
51. K. Sasaki, R. Saito, Progr. Theor. Phys. Suppl. **176**, 253–278 (2008)
52. K. Sasaki, S. Murakami, R. Saito, J. Phys. Soc. Jpn. **75**, 074713 (2006)
53. K. Sasaki, K. Sato, R. Saito, J. Jiang, S. Onari, Y. Tanaka, Phys. Rev. B **75**(23), 235430 (2007)
54. K. Sasaki, J. Jiang, R. Saito, S. Onari, Y. Tanaka, J. Phys. Soc. Jpn. **76**, 033702 (2007)
55. M. Igami, M. Fujita, S. Mizuno, Appl. Surf. Sci. **130–132**, 870 (1998)
56. R. Saito, T. Takeya, T. Kimura, G. Dresselhaus, M.S. Dresselhaus, Phys. Rev. B **59**, 2388–2392 (1999)
57. W. Ren, R. Saito, L. Gao, F. Zheng, Z. Wu, B. Liu, M. Furukawa, J. Zhao, Z. Chen, H.M. Cheng, Phys. Rev. B **81**, 035412 (2010)
58. K. Sasaki, M. Yamamoto, S. Murakami, R. Saito, M.S. Dresselhaus, K. Takai, T. Mori, T. Enoki, K. Wakabayashi, Phys. Rev. B **80**(15), 155450 (2009)
59. Y. You, Z. Ni, T. Yu, Z. Shen, Appl. Phys. Lett. **93**, 163112–163114 (2008)
60. C. Casiraghi, A. Hartschuh, H. Qian, S. Piscanec, C. Georgi, A. Fasoli, K.S. Novoselov, D.M. Basko, A.C. Ferrari, Nano Lett. **9**(4), 1433–1441 (2009)
61. S. Neubeck, Y.M. You, Z.H. Ni, P. Blake, Z.X. Shen, A.K. Geim, K.S. Novoselov, Appl. Phys. Lett. **97**, 053110–053112 (2010)
62. L.G. Cançado, M.A. Pimenta, R. Saito, A. Jorio, L.O. Ladeira, A. Grüneis, A.G. Souza Filho, G. Dresselhaus, M.S. Dresselhaus, Phys. Rev. B **66**, 035415 (2002)
63. L.G. Cançado, A. Reina Cecco, J. Kong, M.S. Dresselhaus, Phys. Rev. B **77**, 245408 (2008)
64. A. Grüneis, R. Saito, Ge.G. Samsonidze, T. Kimura, M.A. Pimenta, A. Jorio, A.G. Souza Filho, G. Dresselhaus, M.S. Dresselhaus, Phys. Rev. B **67**, 165402 (2003)
65. R. Saito, M. Furukawa, G. Dresselhaus, M.S. Dresselhaus, J. Phys. Condens. Matter **22**, 334208 (2010)
66. L. Wirtz, M. Lazzeri, F. Mauri, A. Rubio, Phys. Rev. B **71**, 241402(R) (2005)
67. R. Saito, T. Takeya, T. Kimura, G. Dresselhaus, M.S. Dresselhaus, Phys. Rev. B **57**, 4145–4153 (1998)
68. R. Saito, G. Dresselhaus, M.S. Dresselhaus, *Physical Properties of Carbon Nanotubes* (Imperial College Press, London, 1998)
69. J. Zhou J. Dong, Appl. Phys. Lett. **91**, 173108 (2007)

UNCORRECTED PROOF

70. K. Sasaki, R. Saito, K. Wakabayashi, T. Enoki, J. Phys. Soc. Jpn. **79**, 044603 (2010)
71. C. Cong, T. Yu, H. Wang, ACS Nano **6**, 3175–3180 (2010)
72. M. Begliarbekov, O. Sul, S. Kalliakos, E.H. Yang, S. Strauf, Appl. Phys. Lett. **97**, 031908 (2010)
73. A. Das, S. Pisana, B. Chakraborty, S. Piscanec, S.K. Saha, U.V. Waghmare, K.S. Novoselov, H.R. Krishnamurthy, A.K. Geim, A.C. Ferrari, A.K. Sood, Nat. Nanotechnol. **3**, 210–215 (2008)
74. W. Kohn, Phys. Rev. Lett. **2**, 393 (1959)
75. T. Ando, J. Phys. Soc. Jpn. **77**, 14707 (2008)
76. J. Yan, E.A. Henriksen, P. Kim, A. Pinczuk, Phys. Rev. Lett. **101**, 136804 (2008)
77. L.M. Malard, D.C. Elias, E.S. Alves, M.A. Pimenta, Phys. Rev. Lett. **101**, 257401 (2008)
78. T. Ando, J. Phys. Soc. Jpn. **75**, 124701 (2006)
79. L.G. Cançado, A. Hartschuh, L. Novotny, J. Raman Spectrosc. **40**, 1420–1426 (2009)
80. L. Novotny B. Hecht, *Principles of Nano-Optics* (Cambridge University Press, Cambridge, 2006)
81. N. Anderson, A. Hartschuh, L. Novotny, Mater. Today **8**(5), 50–54 (2005)
82. A. Hartschuh, Angew. Chem. Int. Ed. **47**, 8178–8191 (2008)
83. T. Yano, Y. Inouye, S. Kawata, Nano Lett. **6**(6), 1269–1273 (2006)
84. T. Yano, P. Verma, S. Kawata, Y. Inouye, Appl. Phys. Lett. **88**, 093125–093127 (2006)
85. S.S. Kharintsev, G.G. Hoffmann, P.S. Dorozhkin, G.de With, J. Loos, Nanotechnology **18**, 315502–315510 (2007)
86. A. Hartschuh, E.J. Sánchez, X.S. Xie, L. Novotny, Phys. Rev. Lett. **90**, 095503–095506 (2003)
87. N. Anderson, A. Hartschuh, L. Novotny, J. Am. Chem. Soc. **127**, 2533–2537 (2005)
88. N. Anderson, A. Hartschuh, L. Novotny, Nano Lett. **7**(3), 577–582 (2007)
89. I.O. Maciel, N. Anderson, M.A. Pimenta, A. Hartschuh, H. Qian, M. Terrones, H. Terrones, J. Campos-Delgado, A.M. Rao, L. Novotny, A. Jorio, Nat. Mater. **7**, 878–883 (2008)
90. L. Novotny S.J. Stranick, Annu. Rev. Phys. Chem. **57**, 303–331 (2005)
91. A. Hartschuh, M.R. Beverluis, A. Bouhelier, L. Novotny, Philos. Trans. R. Soc. London A **362**, 807–819 (2004)
92. L.G. Cançado, A. Jorio, A. Ismach, E. Joselevich, A. Hartschuh, L. Novotny, Phys. Rev. Lett. **103**, 186101–186104 (2009)

UNCORRECTED PROOF

AUTHOR QUERIES

AQ1. The first author has been considered as corresponding author. Please check.
AQ2. Please provide email address for the corresponding author.
AQ3. Please check whether the edited sentence “Characterization of the...” retains the intended meaning.
AQ4. Please complete and update Refs. [9, 26, 34].

UNCORRECTED PROOF